Version of Record: https://www.sciencedirect.com/science/article/pii/S1352231023004144
Manuscript_5610cb550c5b31fd3b64591db41013d2

# Atmospheric heating in the US from Saharan dust: tracking the June 2020 event with surface and satellite observations.

Manisha Mehra [a], Sujan Shrestha [a], Krishnakumar AP [a], Meghan Guagenti [a], Claire E. Moffett [a, #], Sarah Guberman VerPloeg [a], Melinda A. Coogan [a], Mukesh Rai [b], Rajesh Kumar [c], Elisabeth Andrews [d, e], James P. Sherman [f], James H. Flynn III [g], Sascha Usenko [a], Rebecca J. Sheesley [a, *]

[a] Department of Environmental Science, Baylor University, Waco, TX, USA

[b] Greenhood Nepal, Kathmandu, Nepal

[c] Research Application Laboratory, National Center for Atmospheric Research, Boulder, Colorado, USA

[d] Cooperative Institute for Research in Environmental Sciences, University of Colorado, Boulder, Colorado, USA.

[e] Global Monitoring Laboratory, National Oceanic and Atmospheric Administration, Boulder, Colorado, USA.

[f] Department of Physics and Astronomy, Appalachian State University, Boone, North Carolina, USA

[g] Department of Earth and Atmospheric Sciences, University of Houston, Houston, TX, USA

[#] now at: Atmospheric Science & Technology Division, Pacific Northwest National Laboratory, Richland, WA, USA

*Correspondence to: Rebecca J. Sheesley (Rebecca_Sheesley@baylor.edu)



© 2023 published by Elsevier. This manuscript is made available under the Elsevier user license
https://www.elsevier.com/open-access/userlicense/1.0/

## Highlights

- Impact of June 2020 Saharan dust event (SDE) on aerosol optical properties in the US.
- The June 2020 SDE caused heating of the atmosphere at a rate of up to 0.24 K $day^{-1}$.
- Radiative impacts of SDE are critical for accurate prediction of climate change in the US.

## Graphical Abstract

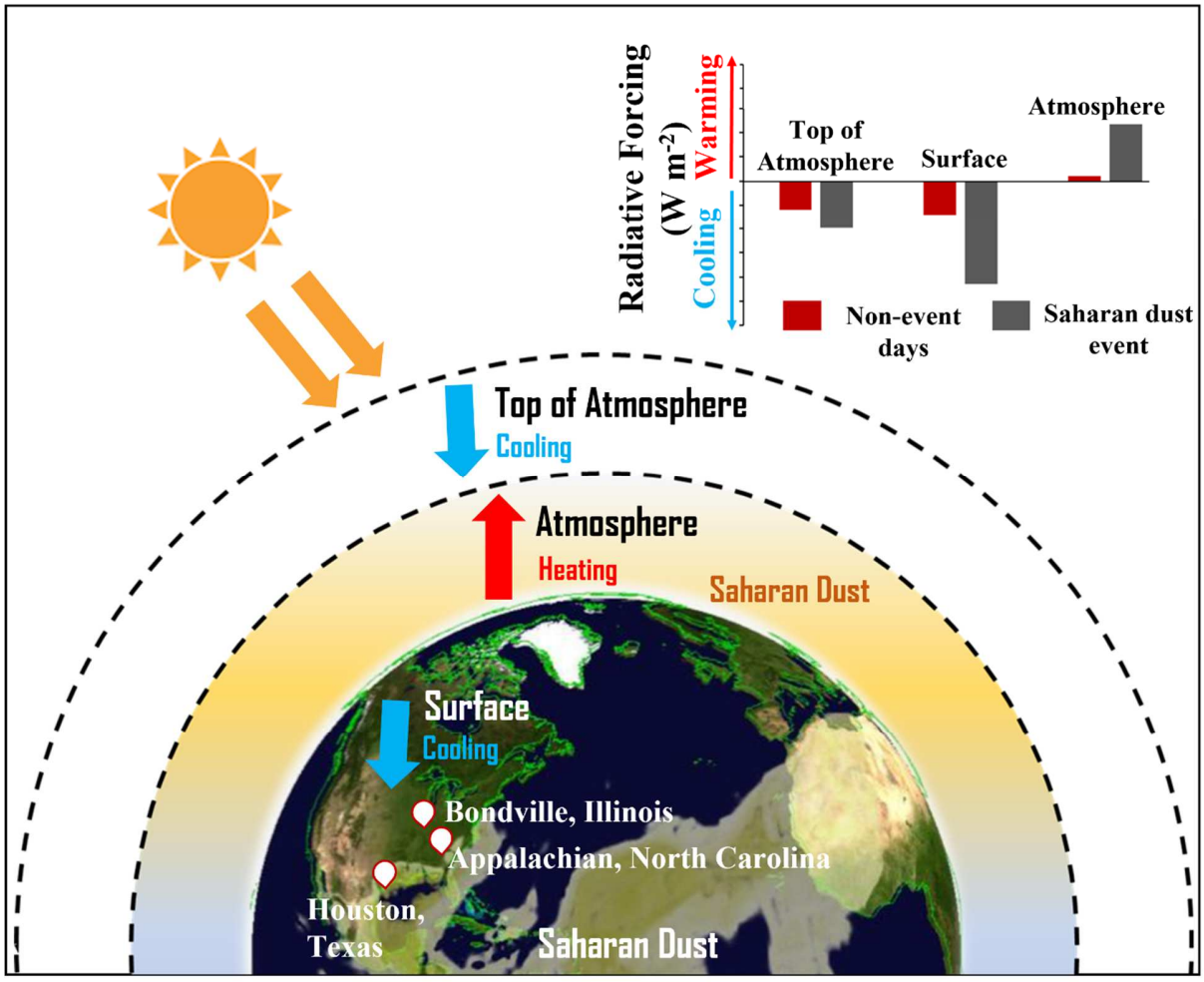

## Abstract

In June 2020, a record level of Saharan dust was transported across the Atlantic Ocean impacting air quality in the Caribbean Basin and the United States (US). Satellite images showed the transport, while a series of ground-based monitoring stations captured the surface impacts as the Saharan dust was transported to the Caribbean basin and then moved into the Southern (Houston, Texas; WL), Eastern (Bone, North Carolina; APP) and Midwestern (Bondville, Illinois; BND) US. The present study characterizes the Saharan dust event (SDE) using a comprehensive set of satellite observations and in-situ measurements of particulate matter (PM), and aerosol optical properties (AOPs; $\sigma_{scat}$: scattering coefficient, $\sigma_{abs}$: absorption coefficient, SAE: scattering Ångström exponent and AAE: absorption Ångström exponent). The Saharan dust intrusion was identified at each site by a marked increase in $\sigma_{scat}$, and AAE and a simultaneous decrease in SAE. A maximum hourly average $PM_{2.5}$ concentration and $\sigma_{scat}$ (525 nm) of 97.5 µg $m^{-3}$ and 190 $Mm^{-1}$ was observed at WL during the SDE. The maximum hourly average $\sigma_{scat}$ (550 nm) for $PM_{10}$ size cut of 215 and 66.9 $Mm^{-1}$ was observed at APP and BND, respectively, during the SDE. The AAE at each site reached above 1.3 with an average value of 1.39±0.35, 3.34±0.56 and 1.65±0.27 at WL, APP, and BND, respectively, during the SDE, whereas the average SAE dropped below 0.5 at WL and APP and below 0.9 at BND. The results demonstrated that the identification of SDE using AOPs depends largely on the location of the measurement, which determines the background characteristics of a site. The results suggest that other intensive AOPs like asymmetry parameter (g) and single scattering albedo Ångström exponent (SSAAE) can also be exploited to characterize SDE. Aerosol radiative forcing (ARF) estimates indicate that the SDE resulted in the heating of the atmosphere (+5.37 to +11.8 W $m^{-2}$) at the rate of 0.11 to 0.24 K $day^{-1}$ at the US sites. This atmospheric heating from transported Saharan dust can alter the

regional atmospheric dynamics and is relevant to understand potential changes in regional climate.

*Keywords:* Saharan dust, continental US, aerosol optical properties, radiative forcing

## Introduction

The trans-Atlantic transport of Saharan dust to the Caribbean basin and North America is an annually recurring phenomenon (Prospero et al., 2014; Yu et al., 2015). It is estimated that approximately 180 million metric tons of Saharan dust is transported each year across the Atlantic Ocean (Francis et al., 2020; Yu et al., 2015; Yu and Zhang, 2013). These Saharan dust events (SDEs) are considered a natural hazard with serious implications on air quality, Earth's radiation budget, cloud and weather systems, and terrestrial and aquatic ecosystems (DeMott et al., 2003; Evan et al., 2011; Jickells et al., 2005; Miller et al., 2004; Song et al., 2018; Yu et al., 2015; Yuan et al., 2016). The frequency and intensity of these SDEs are projected to increase in the future due to changes in land use patterns affecting dust emissions in the Sahara region and circulation patterns favoring the westward transport of African dust (Pu and Jin, 2021; Raj et al., 2019; Taylor et al., 2013). This makes it critical to understand the impact of SDEs on air quality and climate in the downwind regions.

Saharan dust can alter the Earth's radiation budget either directly by scattering and absorbing solar radiation or indirectly by altering the cloud optical properties (Choobari et al., 2014; Francis et al., 2021; Haywood et al., 2005; Prakash et al., 2015). The magnitude and sign of the aerosol radiative forcing strongly depends on the optical properties and size distribution of the dust source (Papadimas et al., 2012; Soupiona et al., 2020). An accurate representation of changes in aerosol optical properties (AOPs) is important for climate models to better estimate the aerosol

impact on climate forcing. However, considerable uncertainties exist in quantifying the impact of Saharan dust on global and regional climate due to limited measurements of aerosol optical, chemical, and microphysical properties (Ryder et al., 2013; Sannino et al., 2022; Soupiona et al., 2020).

In late June 2020, a particularly large SDE was observed in the Caribbean basin and the US (Francis et al., 2021; Pu and Jin, 2021; Yu et al., 2021). The development of a subtropical high-pressure system over the western Saharan desert and a cut-off low-pressure system over the Atlantic Ocean resulted in high northeasterly winds over the Sahara Desert, which favored westward transport of record-level dust, making it one of the largest SDE observed in the last two decades (Francis et al., 2021, 2020; Pu and Jin, 2021). Transport of the Saharan dust was monitored via satellite observations while a series of ground-based aerosol optical monitoring stations captured the influence of the SDE on surface in-situ AOPs in the US. In the present study, real-time AOPs from three ground-based monitoring stations: (i) Southern US (West Liberty, Houston, Texas; WL), (ii) Eastern US (Appalachian State University, Boone, North Carolina; APP), and (iii) Midwestern US (Bondville, Illinois; BND) are used to characterize transport and impacts of Saharan dust in these downwind regions. The main aim of this study is (i) to evaluate the feasibility of using AOPs for near real-time detection of the SDE at these specific sites, each with different background conditions and, (ii) to estimate the impact of SDE on the regional radiation budget. It should be noted here that the primary objective of the study is to detect dust by analyzing the changes in the AOPs at each site. This approach allows us to gain insight into the local variations and effects of Saharan dust on AOPs at each specific location. In what follows, Section 2 describes the surface locations where AOPs were measured, summarizes instrumentation used for measuring AOPs and the satellite data used for characterizing the 2020 SDE, and, finally,

117 presents an overview of the model used for estimating the impact of the SDE on radiative forcing.
118 Section 3 presents major results of the in-situ, satellite data analysis and model outputs and
119 addresses important questions including: (i) relevance of SDE for air quality and (ii) impact of
120 SDE on radiative properties of aerosols and associated forcing. Major conclusions are presented
121 in Section 4.

122 **2. Methodology**

123 **2.1 Site description**

124 This study investigates AOPs at three different monitoring stations: WL, APP, BND.
125 The Texas site (WL) is part of the newly developed Texas Commission on Environmental
126 Quality (TCEQ) Black and Brown Carbon (BC2) network in Texas. The APP and BND sites are
127 part of the National Oceanic and Atmospheric Administration (NOAA) Federated Aerosol
128 Monitoring Network (NFAN) (Andrews et al., 2019). Some additional information about the
129 study sites is presented in Table 1 and their geographic locations are marked in Figure 1. More
130 details about each site are discussed in the Supplementary section S1.

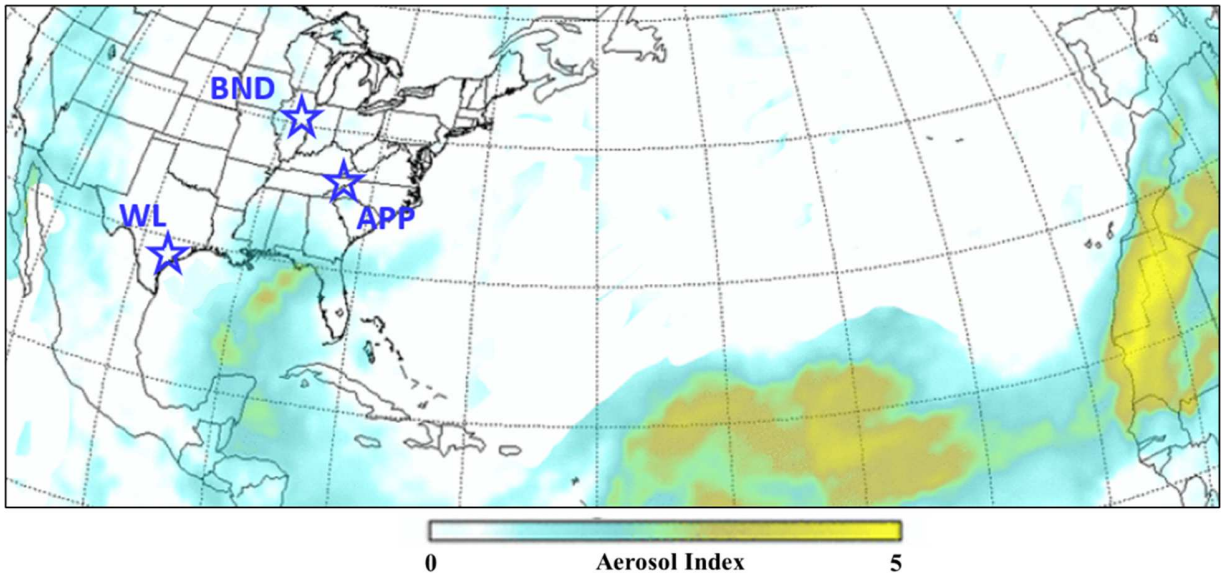


131 **Figure 1.** Spatial distribution of average aerosol index [AI] retrieved from Suomi NPP OMPS
132 for June 25 & 26, 2020 *[Source: NASA/NOAA]*. A dense dust plume is observed over the eastern,
133 central Atlantic and the Caribbean Basin with AI above 3. The geographical locations of the BC2
134 site (WL) and the NFAN monitoring sites (APP and BND) are also shown.

135 **Table 1.** Monitoring site locations and descriptions.

| Site name and location | Site abbreviation | Latitude, Longitude, Altitude (m.agl) | Site classification | Network/Funding |
|---|---|---|---|---|
| West Liberty, Texas, USA | WL | +30.05724°, -94.97829°, 9.0 | Semi-rural | Black and Brown Carbon (BC2) Monitoring Network/ Texas Commission on Environmental Quality |
| Appalachian State University, Boone, North Carolina, USA | APP | +36.2000°, -81.7000°, 1080 | Semi-rural | NOAA Federated Aerosol Network |
| Bondville, Illinois, USA | BND | +40.0519°, -88.373°, 230 | Semi-rural | NOAA Federated Aerosol Network |

136

## 2.2 Measurement and instrumentation

All three sites employ a similar suite of instrumentation: an integrating nephelometer and filter-based absorption photometer, both of which measure at three visible wavelengths. Specifics of the instrumentation for both BC2 and the NFAN sites are discussed in detail in section 2.2.1. It should be noted that the measurements at APP and BND began in 2009 and 1994, respectively whereas, measurements at WL began June 24, 2020, two days before the SDE impacted the site.

### *2.2.1 Measurement of the extensive aerosol optical properties*

#### *2.2.1.1 Aerosol scattering measurements*

At the BC2 site (WL), the aerosol light scattering ($\sigma_{scat}$) and backscattering ($\sigma_{bscat}$) coefficients were measured using a LED-based integrating nephelometer (model Aurora 3000, ECOTECH) at 450, 525 and 635 nm. Calibration of the nephelometer was performed prior to the instrument deployment at the site and then every 15 days using $CO_2$ as a span gas with known Rayleigh scattering factor. Zero checks were performed once every week by using internally filtered particle-free air passed through a High Efficiency Particulate Air (HEPA) filter. A relative humidity (RH) threshold (RH<40 %) was set following the World Meteorological Organization Global Atmospheric Watch guidelines (WMO, 2011). The nephelometer data was reported every 5s and was logged using DAQfactory Pro (AzeoTech Inc.)

At the NFAN sites (APP and BND) a TSI integrating nephelometer (model 3563) was used to measure the $\sigma_{scat}$ and $\sigma_{bscat}$ coefficients at 450, 550, and 700nm. Zero checks on the nephelometers occurred hourly and $CO_2$ span checks were performed approximately monthly. As with the WL site, the NFAN measurements were made at low RH (<40%). Data was reported every second but averaged to 1 min by the NOAA data acquisition system before logging.

159 The ECOTECH and TSI Nephelometer data was corrected for truncation and other
160 instrument non-idealities based on Müller et al. (2011) and Anderson and Ogren (1998),
161 respectively and further averaged to 1 h after correction and QA/QC for each site. The BC2 site
162 measures scattering (and absorption) at $PM_{2.5}$ size cut. The NFAN sites measure scattering (and
163 absorption) at two size cuts ($PM_{10}$ and $PM_1$) but only the $PM_{10}$ measurements are used in the
164 analysis discussed here. The measurements in $PM_1$ size cut at APP and BND were used to
165 perform the sensitivity analysis to assess the impact of particle size cut on the detection of SDE
166 using AOPs (discussed in section 3.1.2). More details about the operational and calibration
167 processes at the NFAN sites are discussed by Andrews et al. (2019).
168 *2.2.1.2 Aerosol absorption measurements*

169 At the BC2 site (WL), the absorption coefficient ($\sigma_{abs}$) was measured using the tricolor
170 absorption photometer (TAP; Model 2901, Brechtel Inc., Hayward, CA) at 365, 520 and 640 nm.
171 The TAP is a commercially available version of NOAA's Continuous Light Absorption
172 Photometer (CLAP) (described below) and uses ten solenoid valves to consecutively sample
173 through eight sample filter spots and two reference filter spots on a 47-mm, glass-fiber filter
174 (TAP-FIL100-EM, Pall Emfab) (Ogren et al., 2017). The TAP automatically advances to the
175 next filter spot when the filter transmittance drops to 70%. The BC2 site utilizes two TAPs
176 operating alternatively every hour in order to reduce the manual efforts such as frequent site
177 visits for changing the TAP filters. The TAPs were intercompared prior to the deployment at WL
178 and again every 15 days for at least 24 hours. The TAP measures $\sigma_{abs}$ every second which was
179 later averaged over an hour and used in this study. TAP data acquisition was performed using the
180 TAP software provided by Brechtel. At the NFAN sites (APP and BND), the $\sigma_{abs}$ at wavelengths
181 467, 528, and 652 nm was measured using a three-wavelength CLAP (Andrews et al., 2019;

Ogren et al., 2017). The CLAP uses 47 mm diameter, glass-fiber filters (Pallflex type E70-2075W) for sampling (Ogren et al., 2017). As with the nephelometer, the CLAP data was reported every second, averaged to 1 min resolution before logging and hourly-averaged before use in this study.

The raw absorption values obtained from the TAP and CLAP were corrected for individual instrument discrepancies related to issues like spot size and flow as well as for artifacts related to aerosol scattering due to filter type (Bond et al., 1999; Ogren, 2010). It should be noted that the Pall Emfab filters used in the TAP were found to perform similar to the original Pall E70 filters used in the CLAPs with only a 7% correction. This correction was applied to the TAP data from BC2-WL. Previous studies have extensively employed similar correction schemes with TAP/CLAP to investigate the aerosol absorption properties under wide range of sampling conditions including impact of wildfire emissions and African dust (Collaud Coen et al., 2020; Davis et al., 2019; Denjean et al., 2016; Farah et al., 2020; May et al., 2023; Shrestha et al., 2023; Sorribas et al., 2019, 2017; Torres-Delgado et al., 2021). However, it is important to highlight that the particle size is known to affect many of the correction schemes utilized for filter-based absorption measurements (e.g., Bond et al., 1999; Yus-Díez et al., 2020). This is an active area of research in the aerosol absorption community, but this specific aspect was not evaluated in this study. The $\sigma_{abs}$ for each site were adjusted (using the calculated absorption Ångström exponent) to match the co-located nephelometer wavelengths, i.e., 450, 525 and 635 nm for the BC2 site and 450, 550 and 700nm for NFAN sites.

*2.2.2 Calculation of the intensive aerosol optical properties*

The measured extensive AOPs were used for calculating the intensive AOPs such as Scattering Ångström Exponent (SAE), Absorption Ångström Exponent (AAE), asymmetry parameter (g),

205 single scattering albedo (SSA) and single scattering albedo Ångström exponent (SSAAE). The
206 extensive and intensive AOPs and the equations used to derive the intensive AOPs are reported
207 in Table S1 and are briefly discussed in supplementary section S2.

208 *2.3. Particulate Matter Measurements and Enrichment Factor*

209 The real time hourly average mass concentrations of $PM_{2.5}$ and $PM_{10}$ for the Houston-Galveston
210 region were taken from the TCEQ Texas air quality monitoring network
211 (https://www.tceq.texas.gov/gis/geotam-viewer; Section 3.1 and 3.3). The network utilizes a
212 Tapered Element Oscillating Microbalance (TEOM) for measuring PM concentration.

213 At APP, a TEOM provided by the North Carolina Department of Environmental and
214 Natural Resources Division of Air Quality, is used measure PM mass concentrations. The details
215 about the sampling set up at APP is described in supplementary section S3. The $PM_{10}$
216 concentrations for BND were taken from the Interagency Monitoring of Protected Visual
217 Environment Network (IMPROVE) network. The 24-hour PM samples in different size bins
218 ($PM_{2.5}$ and $PM_{10}$) are collected gravimetrically, every three days at the IMPROVE sites. More
219 details about the network can be found at http://vista.cira.colostate.edu/Improve.

220 *2.4. Enrichment Factor*

221 One of the TCEQ Texas air quality monitoring sites in Houston (Deer Park) also collected $PM_{2.5}$
222 aerosol filter samples. The aerosol samples were analyzed for the elemental composition using
223 energy dispersive X-ray fluorescence spectrometry. In this study we have used the
224 concentrations of select elements (Al, As, Ba, Ca, Co, Cr, Fe, K, Mg, Mn, Na, Ni, P, Rb, Se, Si,
225 Sr, Zn), obtained from $PM_{2.5}$ samples collected at Deer Park, to calculate Enrichment Factors
226 (EF) for Houston PM during the SDE. Details about the EF calculations are discussed in the
227 supplementary section S4.

228 *2.5. Criteria for Saharan dust event identification*

229 As discussed above, the SAE and AAE can provide vital information about aerosol size
230 and composition. In addition, enhancement of $\sigma_{scat}$ may also considered an effective means of
231 determining the impact of mineral dust for some in-situ sites (Collaud Coen et al., 2004; Ealo et
232 al., 2016; Fernández et al., 2017; Nicolás et al., 2019; Titos et al., 2017). In this study the SDE
233 was identified using combination of extensive ($\sigma_{scat}$) and intensive (SAE and AAE) AOPs at the
234 respective sites. The present study defines a SDE as the time period with both (i) SAE below 0.5
235 and (ii) $\sigma_{scat}$ and AAE exceeding the June average values by more than one standard deviation
236 for more than 4-hour duration at WL and APP. The $\sigma_{scat}$ at BND looked similar during SDE and
237 non-event days so the SDE is defined based on SAE and AAE. The time period with SAE<0.9
238 and AAE exceeding the June average values by more than one standard deviation for more than
239 4-hour duration was defined as SDE at BND. Since the WL site began observations at the very
240 end of June (discussed in section 2.2.1.1), an average $\sigma_{scat}$ and AAE for the period between June
241 26 to July 31 was used in lieu of a monthly average to identify the SDE. The cutoff for SAE, $\sigma_{scat}$
242 and AAE to identify the SDE at each site is presented in Table S2. The cutoff values for the
243 SAE, $\sigma_{scat}$ and AAE are entirely conservative for this specific SDE at each site.
244 Previous studies have also used an increase in aerosol optical depth (AOD), and PM
245 concentration accompanied by a decrease in SAE as an indicator of mineral dust at different sites
246 around the globe such as those in north-western Mediterranean, Iberian Peninsula, Spain (Ealo et
247 al., 2016; Fernández et al., 2017; Titos et al., 2017; Valenzuela et al., 2015). Therefore, we have
248 used the Moderate Resolution Imaging Spectroradiometer (MODIS) retrieved AOD and PM
249 measurements for all the sites to corroborate the identified SDE. The details about the AOD
250 retrieval and analysis are discussed in supplementary section S5. Based on the defined criteria,

the 2020 SDE was identified between June 26-27 at WL, June 27-28 at APP, and June 28-29 at BND, respectively (discussed in detail in section 3.1). It is worth highlighting here that changes in the intensive AOPs (e.g., AAE and SAE) were observed before our constraints identified SDE at the study sites. This highlights the greater sensitivity of intensive AOPs to variations in aerosol physical and chemical characteristics. In contrast, there was little change in the PM concentration and $\sigma_{scat,}$ during the time leading up to the SDE at any site. Since, the focus of the study was to primarily detect a significant event with a substantial impact on the air quality, this transitional period was not included in the defined SDE at the study sites. This transition period at each site is shaded in a different color to distinguish it from the defined SDE (Figure 2 & 3).The days not identified as the SDE between June 20 and 30, 2020 were considered as representative of non-event days. It should be noted that WL, APP and BND experienced rainfall amidst the SDE (on June 27, June 28, and June 29, respectively). This resulted in lower $\sigma_{scat}$, $\sigma_{abs}$ and AAE and higher SAE than the cut off values for SDE identification for several hours (~ 7 hours) at the study sites.

*2.6 Aerosol Radiative Forcing*

The impact of Saharan dust on the aerosol radiative forcing (ARF) was calculated using a two-step methodology. This approach involved (i) derivation of columnar AOPs (AOD, SSA, and g) and their spectral variation using the Optical Properties of Aerosols and Clouds (OPAC) model (Hess et al., 1998) and then (ii) using these derived columnar spectrally varying AOPs in the Santa Barbara Discrete Ordinate Atmospheric Radiative Transfer (SBDART) model (Ricchiazzi et al., 1998) to calculate the ARF. A similar approach has been extensively used in previous studies to investigate the impact of mineral dust on the radiation budget (Dumka et al., 2016; Kaskaoutis et al., 2013, 2019; Kumar et al., 2015; Li et al., 2020). It should be noted that the

surface observations of AOPs were not directly used in these simulations. The details of the model simulations are presented in supplementary Section S6.

## 3. Results and Discussion

### 3.1 Characterization of the 2020 Saharan dust event using aerosol optical properties

Ground-based AOP measurements and satellite retrievals were used to characterize a SDE and dust transport across the United States during June 2020. The temporal variability in scattering ($\sigma_{scat}$) and absorption ($\sigma_{abs}$) coefficients measured at WL ($PM_{2.5}$ size cut) and at APP and BND ($PM_{10}$ size cut) is presented in Figure 2 and Figure S1. Figures 3 and 4 presents the variability in the SAE, AAE, SSA and SSAAE at the study sites. The detailed statistics of the AOPs observed during the SDE, identified using the criteria discussed above, is presented in Table 2. The AOPs at each site during the SDE are also compared with those observed during the non-event days to better characterize the influence of Saharan dust. Statistically significant differences were measured in the AOPs across the sites for the SDE vs non-event days, indicating the strength of the identification of the SDE using these parameters. When available, the PM mass concentrations and AOD can further indicate the magnitude of the dust impacts at the different sites.

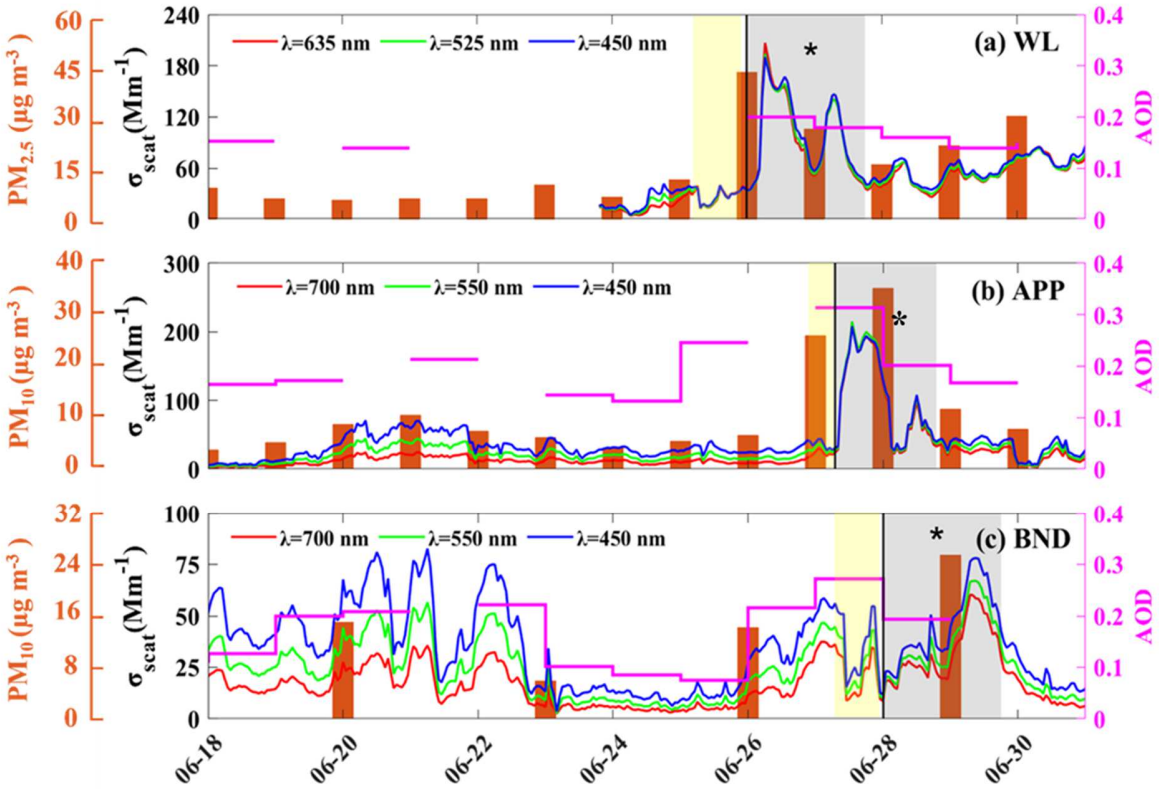


**Figure 2.** Time series of hourly average scattering coefficient ($\sigma_{scat}$) at (a) West Liberty (WL) (b) Appalachian State University (APP) (c) Bondville (BND) (left axis). Measurements at WL are of $PM_{2.5}$ aerosols and at APP and BND are of $PM_{10}$ aerosols. The bar graph shows the daily average mass concentrations of $PM_{2.5}$ at (a) WL, and $PM_{10}$ at (b) APP and (c) BND (left axis). The right y axis shows the daily average AOD for a 0.5° × 0.5° grid centered over each site. The solid vertical line indicates onset of the dust influence at the study sites. The gray shaded area represents the SDEs identified at each site. The yellow shaded area represents the transition period from non-event days to SDE. The asterisk sign represents the time period when the sites experienced precipitation resulting in lower $\sigma_{scat}$ than the cut off value during the SDE.

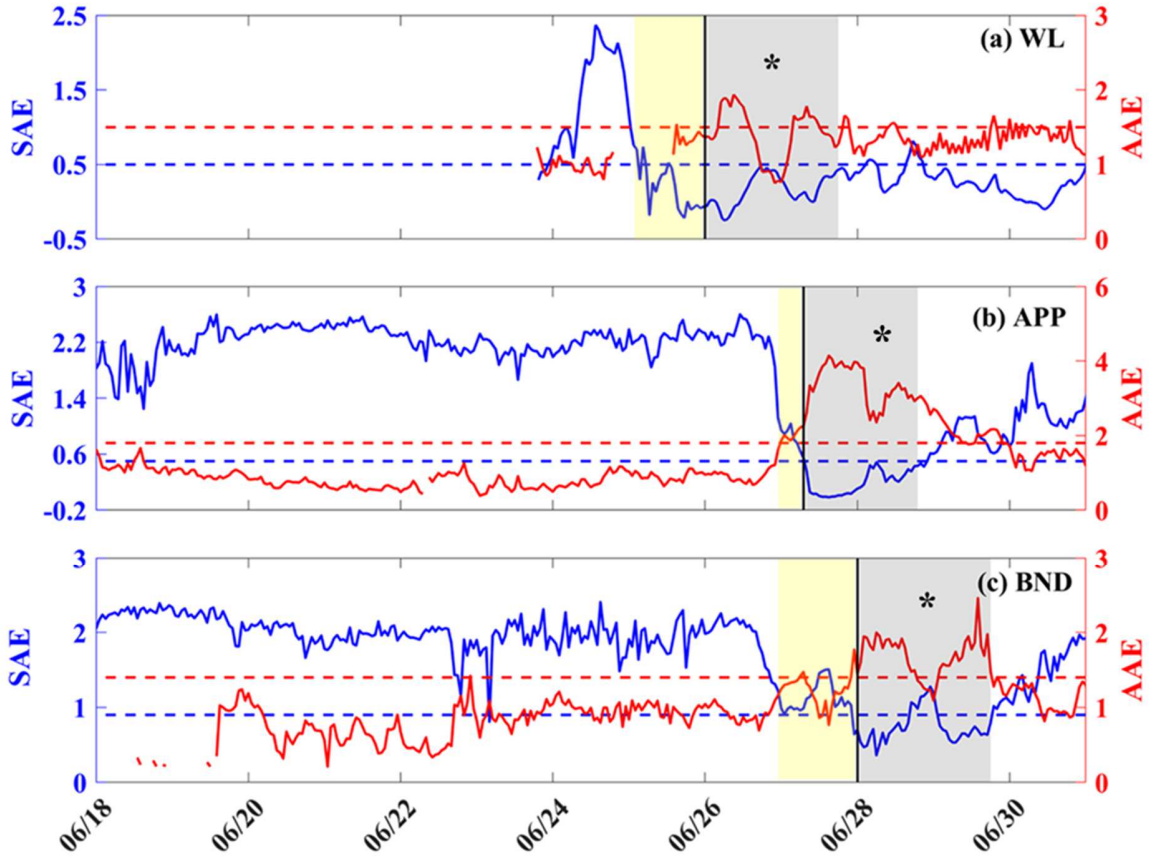


**Figure 3.** Times series of hourly average SAE and AAE at (a) West Liberty (WL) (b) Appalachian State University (APP) (c) Bondville (BND). The solid vertical line indicates onset of the dust influence at the study sites. The gray shaded area represents the SDE identified at each site. The yellow shaded area represents the transition period from non-event days to SDE. The dashed blue and red horizontal line show the cutoff for SAE (0.5 at WL, APP and 0.9 at BND) and AAE (1.5 at WL, 1.8 at APP and 1.4 at BND), respectively for dust identification. Measurements at WL were of $PM_{2.5}$ aerosols and at APP and BND were of $PM_{10}$ aerosols. Note the different y-axis scales for each site. The asterisk sign represents the time period when the sites experienced precipitation during the SDE.

**Table 2.** Basic statistics of the measured extensive and calculated intensive aerosol optical properties at the study sites during the Saharan dust event and non-event days.

| Site | Parameter | Wavelength (nm) | Saharan dust event[a] | | | Non-event days[b] | | | p-value[c] |
|---|---|---|---|---|---|---|---|---|---|
| | | | Mean ± 1σ | Min | Max | Mean ± 1σ | Min | Max | |
| WL | $PM_{2.5}$ (μg $m^{-3}$) | - | 37.9±23.2 | 10.3 | 97.5 | 15.1±6.98 | 1.95 | 43.0 | <0.05 |
| | $\sigma_{scat}$ ($Mm^{-1}$) | 635 | 98.2±48.1 | 34.5 | 207 | 34.5±13.3 | 6.43 | 69.3 | <0.05 |
| | | 525 | 98.4±45.9 | 33.5 | 194 | 39.3±13.8 | 7.46 | 78.9 | <0.05 |
| | | 450 | 102±45.9 | 33.8 | 190 | 45.3±15.6 | 8.51 | 91.1 | <0.05 |
| | $\sigma_{abs}$ ($Mm^{-1}$) | 635 | 8.73±4.18 | 3.59 | 18.49 | 4.68±1.36 | 1.62 | 8.45 | <0.05 |
| | | 525 | 9.19±4.36 | 3.81 | 19.32 | 5.00±1.49 | 1.54 | 9.20 | <0.05 |
| | | 450 | 9.49±4.53 | 3.71 | 19.78 | 5.25±1.64 | 1.42 | 10.2 | <0.05 |
| | g | 525 | 0.68±0.03 | 0.62 | 0.73 | 0.58±0.04 | 0.43 | 0.65 | <0.05 |
| | SAE | 450-635 | 0.15±0.11 | -0.25 | 0.47 | 0.83±0.49 | -0.07 | 1.92 | <0.05 |
| | AAE | 450-635 | 1.39±0.35 | 0.72 | 1.92 | 1.19±0.21 | 0.54 | 2.24 | <0.05 |
| | SSA | 525 | 0.97±0.01 | 0.94 | 0.98 | 0.93±0.03 | 0.74 | 0.97 | <0.05 |
| | SSAAE | 450-635 | -0.04±0.02 | -0.09 | -0.01 | 0.01±0.04 | -0.13 | 0.19 | <0.05 |
| | | | | | | | | | |
| APP | $PM_{10}$ (μg $m^{-3}$) | - | 34.7±23.9 | 8.3 | 77.1 | 7.37±2.47 | 2.95 | 12.2 | <0.05 |
| | $\sigma_{scat}$ ($Mm^{-1}$) | 700 | 104±64.6 | 22.0 | 209 | 14.1±8.42 | 0.46 | 36.6 | <0.05 |
| | | 550 | 108±65.6 | 24.4 | 215 | 22.8±13.7 | 0.42 | 60.7 | <0.05 |
| | | 450 | 108±62.1 | 26.8 | 208 | 34.4±20.8 | 0.64 | 93.9 | <0.05 |
| | $\sigma_{abs}$ ($Mm^{-1}$) | 700 | 1.58±0.83 | 0.52 | 3.01 | 1.44±0.73 | 0.16 | 5.21 | 0.29 |
| | | 550 | 3.90±2.42 | 0.93 | 8.02 | 1.80±0.88 | 0.23 | 6.75 | <0.05 |
| | | 450 | 7.79±5.18 | 1.54 | 16.5 | 2.15±1.01 | 0.31 | 8.24 | <0.05 |
| | g | 550 | 0.63±0.01 | 0.60 | 0.64 | 0.59±0.07 | 0.48 | 0.69 | <0.05 |
| | SAE | 450-700 | 0.19±0.17 | -0.02 | 0.55 | 2.00±0.46 | -0.74 | 2.65 | <0.05 |
| | AAE | 450-700 | 3.34±0.56 | 2.25 | 4.14 | 0.96±0.41 | 0.25 | 3.06 | <0.05 |
| | SSA | 550 | 0.97±0.01 | 0.96 | 0.97 | 0.91±0.05 | 0.61 | 0.97 | <0.05 |
| | SSAAE | 450-700 | -0.11±0.03 | -0.15 | -0.07 | 0.09±0.05 | -0.46 | 1.55 | <0.05 |

| | | | | | | | | | |
|---|---|---|---|---|---|---|---|---|---|
| BND | $PM_{10}$ (µg $m^{-3}$) | - | 25.4[d] | - | - | 13.0±4.83 | 5.86 | 19.5 | <0.05 |
| | $\sigma_{scat}$ ($Mm^{-1}$) | 700 | 31.3±14.1 | 8.68 | 60.2 | 12.9±9.66 | 2.22 | 35.3 | <0.05 |
| | | 550 | 36.3±15.7 | 10.0 | 66.9 | 19.4±14.5 | 2.50 | 50.2 | <0.05 |
| | | 450 | 43.5±18.0 | 11.8 | 78.1 | 28.8±21.0 | 3.57 | 75.3 | <0.05 |
| | $\sigma_{abs}$ ($Mm^{-1}$) | 700 | 1.53±0.96 | 0.48 | 5.35 | 1.79±1.09 | 0.20 | 9.30 | 0.11 |
| | | 550 | 2.24±1.30 | 0.75 | 7.04 | 2.26±1.44 | 0.24 | 11.9 | 0.91 |
| | | 450 | 3.08±1.67 | 1.10 | 8.65 | 2.74±1.84 | 0.33 | 16.9 | 0.22 |
| | g | 550 | 0.66±0.02 | 0.62 | 0.70 | 0.60±0.07 | 0.48 | 0.73 | <0.05 |
| | SAE | 450-700 | 0.76±0.22 | 0.36 | 1.28 | 1.80±0.36 | -0.11 | 2.40 | <0.05 |
| | AAE | 450-700 | 1.65±0.27 | 1.09 | 2.46 | 1.01±0.37 | 0.20 | 1.94 | <0.05 |
| | SSA | 550 | 0.94±0.03 | 0.83 | 0.97 | 0.88±0.06 | 0.66 | 0.99 | <0.05 |
| | SSAAE | 450-700 | -0.04±0.02 | -0.07 | 0.02 | 0.09±0.06 | -0.17 | 0.36 | <0.05 |

[a] Saharan dust event- WL: June 26-27,2020; APP: June 27-28 and BND: June 28-29, 2020

[b] Non-event Day- WL: July 09-20,2020; APP: June 01-26, 2020, and BND: June 01-27, 2020

[c] p-value for two sample t-test

[d] Only one filter sample was collected at the IMPROVE site during the SDE at BND. Therefore, values for standard deviation, minimum and maximum $PM_{10}$ at the site are not reported here.

### *3.1.1 Evolution of Saharan dust plume in the US*

The spatial distribution of AOD (Figure S2) suggests that Saharan dust plumes moved to Texas (Southern US) through the Gulf of Mexico while a branch of dust appeared to enter Florida and other eastern and midwestern states of US starting June 25. Since the BC2 network in Houston, Texas only had one site in operation at the time of the SDE, increases in the MODIS AOD (Figure 2a & S2) and surface $PM_{2.5}$ concentration from other air quality sites in the region (Figure 5 & S3) were used to track the transport of Saharan dust across the region. The initial wave of the SDE reached coastal sites near Houston on June 25, while a second plume of dust was then observed first at the coastal sites, then inland sites (including WL) on June 26 and 27,

2020. A maximum hourly average $PM_{2.5}$ concentration of 97.5 µg $m^{-3}$ and 55.4 µg $m^{-3}$ was observed at WL on June 26 and 27, respectively (Figure 5; discussed in detail in Section 3.3). The daily average $PM_{2.5}$ concentration on June 26 (43.1 µg $m^{-3}$) exceeded the Environmental Protection Agency (EPA) 24-hour National Ambient Air Quality Standard of 35 µg $m^{-3}$ (Figure 5a). The average $\sigma_{scat}$ (525 nm) was 98.4± 45.9 $Mm^{-1}$ with a maximum hourly average of 194 $Mm^{-1}$, while the SAE and AAE of 0.15 ± 0.11 and 1.39 ± 0.35 were observed at WL during this SDE (Figure 2a & 3a; Table 2). Similar SAE and AAE values have also been reported during Saharan dust influence in the Central Mediterranean and Europe (Ealo et al., 2016; Fernández et al., 2017; Gómez-Amo et al., 2011; Nicolás et al., 2019; Pace et al., 2006; Titos et al., 2017)

The Saharan dust reached North Carolina (APP) on June 27 and Illinois (BND) on June 28 (Figure 2b-c & S2). The impact of Saharan dust was more pronounced at APP than at BND. At APP, the average $PM_{10}$ mass concentration and $\sigma_{scat}$ (550 nm) were ~ 5 times higher during the SDE than that observed during the non-event days. A maximum hourly average $PM_{10}$ mass concentration reached to 77.1 µg $m^{-3}$ and 68.8 µg $m^{-3}$ on June 27 and 28, respectively. Average $\sigma_{scat}$ (550 nm) of 108±65.60 $Mm^{-1}$ was observed at APP during the SDE compared to non-event days (June 01-26, 2020) (Figure 2b). Average SAE decreased from 2.00±0.46 to 0.19±0.17 and average AAE increased from 0.96±0.41 to 3.34±0.56 at APP during the SDE compared to non-event days (Figure 3b; Table 2). The site experienced precipitation on the night of June 27 and continued through June 28 resulting in decrease in the $\sigma_{scat}$ and $\sigma_{abs.}$ Despite a significant decrease in $\sigma_{scat}$ and $\sigma_{abs}$ at APP on June 28, the intensive AOPs (AAE, SAE, SSA, SSAAE) did not show any change. This again emphasizes the higher sensitivity of intensive AOPs to the aerosol physical and chemical characteristics. The results also indicate that the APP was predominantly

352 influenced by Saharan dust aerosols even during the precipitation, likely due to lack of other
353 anthropogenic emission sources at this elevated site.
354 At BND, the average 24-hour $PM_{10}$ concentration was 2-fold higher during the SDE
355 compared to non-event days but that is based on a single 24-hour filter collected during the
356 event. The average $\sigma_{scat}$, SAE and AAE were 35.20±14.73 $Mm^{-1}$, 0.88±0.28 and 1.51±0.33,
357 respectively during the SDE (Figure 2c & 3c; Table 2). The difference in the aerosol loading
358 between APP and BND indicated the presence of a non-uniform dust plume. The APP site, being
359 situated at an elevation of 1080 m agl, was influenced by a plume with higher mineral dust
360 loading than that observed at BND (situated at an elevation of 230 m agl) during the SDE.
361 Moreover, the magnitude of the impact of SDE at BND was also likely affected by the wet
362 deposition of dust due to precipitation during the course of transport and/or at the site on June 29.
363 Notably, the SAE at BND during the SDE (average 0.76±0.22) was higher compared to the SAE
364 values observed at the other two sites in this study and those reported in literature during SDEs
365 (Collaud Coen et al., 2004; Ealo et al., 2016; Gómez-Amo et al., 2011; Titos et al., 2017;
366 Valenzuela et al., 2015). BND, a semi-rural site surrounded by soy and corn fields, is influenced
367 by the local fugitive emissions from agricultural activities (Delene and Ogren, 2002; Sherman et
368 al., 2015). Although the peak $\sigma_{scat}$ at BND looked similar during SDE and non-event days, AAE
369 and SAE varied significantly as Saharan dust intruded on the site (Figure 2c & 3c).
370 A SDE can result in a temporary increase in PM concentrations, however, at certain
371 sites, it can also have long-term impacts. The $\sigma_{scat}$ at WL decreased to 60 $Mm^{-1}$ (at 550 nm) on
372 June 28, however, SAE and AAE values remained relatively similar to those observed during the
373 SDE, until July 03 (Figure 3 & S4). This consistency in the SAE and AAE suggests that the site
374 was under the influence of Saharan dust till July 03. Sporadic peaks in $\sigma_{scat}$ were also observed at

WL between June 29 to July 03 with an hourly maximum of 136 $Mm^{-1}$ (at 550 nm) (Figure S4). The statistics of measured AOPs between June 28- July 03 at WL is presented in Table S3. Notably, intermittent dust influence later in the month of July was also observed at WL (Figure S4).

The elemental composition of $PM_{2.5}$ aerosols collected at the TCEQ site Deer Park in the months of May, June and July were also analyzed (discussed in detail in Section 3.3). The enrichment factors (EF) for selected anthropogenically emitted elements were reduced by ~90% during the SDE and were also diluted for the samples collected later in the month of July suggesting further influence of dust (Figure S5 & S6). This can be linked to the on-going transport of a secondary Saharan plume with lower concentrations of dust to Houston. Relatively higher AOD over the Gulf of Mexico between June 28 to 30 (Figure S2) further substantiate the possible transport of a secondary dust plume to the Houston sites. In addition, dry summer conditions can also facilitate the recirculation and/or re-suspension of Saharan dust in the atmosphere after the dust event and may result in low SAE and high AAE values during the month of July at WL. A previous study by Bozlaker et al. (2013) used a chemical mass balance (CMB) receptor model to isolate multiple sources of mineral contributing to ambient aerosol loading during long-range transport of Saharan dust to Houston during summer 2008. Although the SDE lasted for a couple of days, the CMB model indicated that Saharan dust was present as a substantial "background" aerosol component for multiple days due to the recirculation and/or re-suspension of dust even after the SDE. The evidence that mineral dust can continue to recirculate and/or be re-suspended in the atmosphere under dry conditions in summer after the initial SDE is of high relevance for air quality. More studies are needed to separate the impact of recirculated and/or re-suspended dust from on-going dust transport.

The detection of the SDE was different at each site in this study based on differences in local background sources, however, the combination of PM, $\sigma_{scat,}$ AAE and SAE was sufficient to identify the influence of the SDE at the surface. The combination of $\sigma_{scat,}$ SAE and AAE was used to identify the SDE at WL and APP. In contrast, SAE and AAE were the conclusive parameters for SDE identification at BND while $\sigma_{scat}$ was not obviously different for SDE and non SDE days. The real time measurements of AOPs presented in the present study provide an efficient means for long term and routine identification of dust events.

3.1.2. *Sensitivity analysis for detection of SDE in fine PM*

Using the $\sigma_{scat}$ and $\sigma_{abs}$ at the NFAN site (APP and BND) for both the $PM_1$ and $PM_{10}$ size cut, a sensitivity analysis was performed to evaluate the impact of PM size cut on detection of SDE based on AOPs. The AOPs for the $PM_1$ size cut exhibited a similar trend to those observed for the $PM_{10}$ size cut at the NFAN sites. By using the same AOP cutoff values, the period identified as the SDE at APP, based on measurements in $PM_{10}$ size cut, closely aligned with that identified using AOPs for $PM_1$ size cut (Figures S7). Although BND showed a significant decrease in SAE and increase in AAE during the SDE for $PM_1$, the magnitude of the change was much lower than that observed for $PM_{10}$ (Figure S8). It should also be noted here that detecting the SDE at BND was comparatively more challenging compared to the other sites even for the $PM_{10}$ size cut. Overall, this sensitivity analysis suggested that the AOPs for $PM_1$ size cut can still provide valuable information about the presence of dust in the atmosphere, even when the influence of Saharan dust on the overall mass concentration is relatively muted. This further supports the decision to focus on studying the effect of Saharan dust on AOPs despite the $PM_{2.5}$ size cut at WL."

**3.2. Impact of Saharan dust on the radiative properties of aerosols**

421 *3.2.1 Asymmetry parameter*

422 The angular distribution of light scattering by the Saharan dust has more forward scatter;
423 compared to non-Saharan dust aerosols (Horvath et al., 2018; 2016). The average g during the
424 SDE was significantly higher than that observed during the non-event days at all the sites (Table
425 2; Figure S9). A g value larger than 0.65 have been reported previously for Saharan dust while a
426 g value for non-dust aerosols is typically less than 0.6 (Horvath et al., 2018). The g values
427 observed at WL, APP and BND were also similar to those reported for other in situ
428 measurements during SDEs (Ealo et al., 2016; Horvath et al., 2018; Ogren et al., 2006). Some of
429 the previous studies have reported limited variability in g for different types of aerosols
430 (anthropogenic, marine, and dust) (Donateo et al., 2018; Ealo et al., 2016), suggesting
431 asymmetry parameter may not be a useful variable for dust characterization. However, in the
432 present study for the sites and SDE event analyzed it appears that the asymmetry parameter can
433 be used to distinguish between aerosol dominated by desert particles and the continental
434 background during these intense SDEs (Figure S9). Providing a measurement-based constraint
435 for g during the SDE is important given that g is commonly used in radiative transfer models
436 (Ogren et al., 2006).

437 *3.2.2 Single scattering albedo*

438 The temporal variation in the SSA (550 nm) observed at different study sites is presented in
439 Figure 4. The SSA values observed at the study sites are comparable to those reported during the
440 Saharan Dust Experiment (Haywood et al., 2005) and other Saharan dust influenced periods
441 (Ealo et al., 2016; Titos et al., 2017; McFarlane et al., 2009). Notably, the SSA values at all the
442 study sites were >0.90 prior to and during the onset of Saharan dust suggesting that the sites are
443 dominated by scattering aerosols even in the absence of dust and that the dust is relatively non-

absorbing. The SSA during the SDE showed a strong spectral variation, with higher values at higher wavelengths at WL, APP and BND suggesting more scattering at higher wavelengths due to coarse particles (Figure S10).

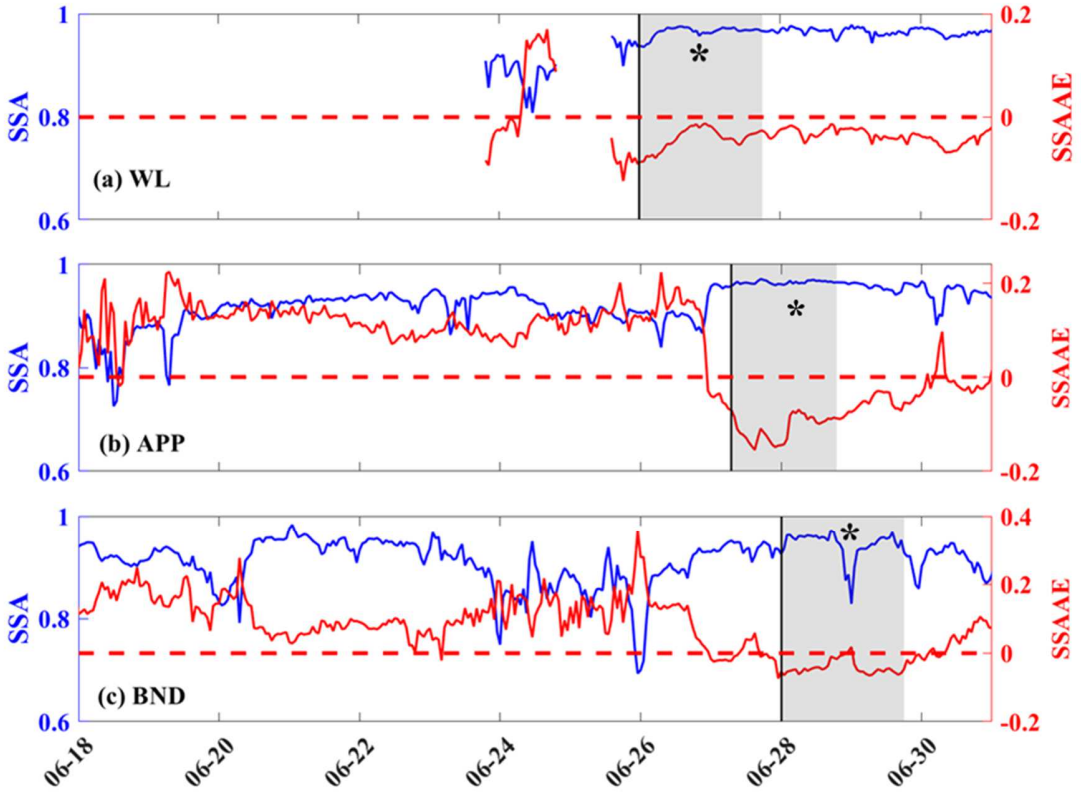


**Figure 4.** Times series of hourly average SSA (550 nm for APP and BND and 525 nm for WL) and SSAAE at **(a)** West Liberty (WL) **(b)** Appalachian State University (APP) **(c)** Bondville (BND). The solid vertical line indicates onset of the dust influence at the study sites. The gray shaded area represents the SDE identified at each site. The dashed red horizontal line shows the SSAAE=0. Measurements at WL were of $PM_{2.5}$ aerosols and at APP and BND were of $PM_{10}$ aerosols. The asterisk sign represents the time period when the sites experienced precipitation during the SDE.

456 The SSAAE ranged between -0.09 to -0.01, -0.15 to -0.07 and -0.07 to 0.06 at WL, APP
457 and BND, respectively during the SDE (Figure 4). During Saharan dust outbreaks, a reduction
458 of SAE and a simultaneous increase in AAE leads to negative SSAAE values depending on the
459 degree of local pollution and intensity of the SDE (Collaud Coen et al., 2004; Ealo et al., 2016).
460 The SSAAE at WL remained negative even later in the month of July corroborating intermittent
461 influence of dust either from on-going transport or from the suspended dust particles(Figure S4).
462 Overall, our results show that SSAAE can also be used together with $\sigma_{scat}$, SAE and AAE to
463 characterize presence of dust at different locations in order to identify presence of Saharan dust
464 in real time.

465 **3.3 Transport of dust across Houston metropolitan area and its relevance for urban air**
466 **quality**

467 The hourly average $PM_{2.5}$ concentrations measured at five different TCEQ air quality monitoring
468 sites in Houston (Figure 5a) were examined for the month of June. The geographic locations of
469 the TCEQ air quality monitoring sites in Houston are shown in Figure S3. $PM_{10}$ concentrations
470 were available for two TCEQ sites (Deer Park and Oyster Creek) in Houston. The Saharan dust
471 entered Texas through the Gulf of Mexico impacting the coastal sites, Galveston and Oyster
472 Creek late (2230 LST) on June 24 (Figure 5a). The maximum hourly average $PM_{2.5}$
473 concentration reached 60 $\mu g\ m^{-3}$ at these coastal sites on June 25 around 0130 LST. A two-fold
474 increase in $PM_{10}$ concentration was observed at Oyster Creek (>150 $\mu g\ m^{-3}$) during the same
475 time. The dust plumes travelled at a speed of ~25 km $hr^{-1}$ and reached an inland site: Deer Park
476 resulting in peak $PM_{2.5}$ and $PM_{10}$ concentration around 0200 LST. The speed of dust transport
477 from the coastal sites to this inland site agreed with average wind speed at these locations. The
478 hourly average PM concentrations showed that the coarse fraction ($PM_{10}$-$PM_{2.5}$) constituted 62%

and 52% of the total $PM_{10}$ concentration at Oyster Creek and Deer Park, respectively with the onset of Saharan dust on June 25 (Figure 5b). The TCEQ monitoring sites located further inland in Houston did not report an increase in $PM_{2.5}$ on June 25. In addition, a drop in PM concentrations was observed in the afternoon on June 25. This is likely due to wet deposition of dust by precipitation later in the day.

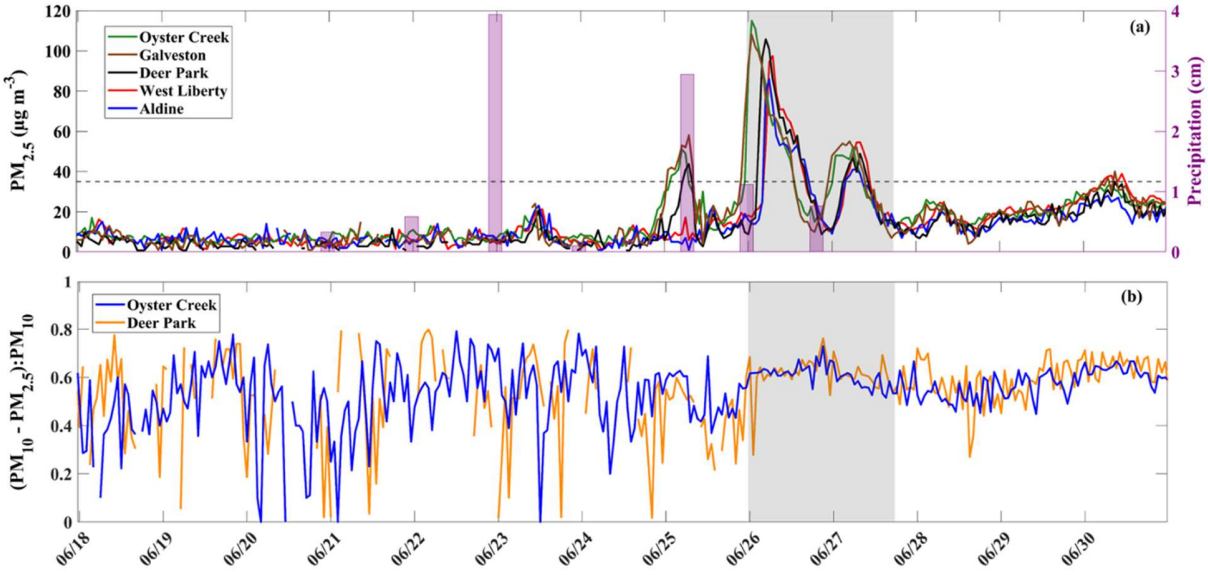


**Figure 5.** Times series of hourly average **(a)** $PM_{2.5}$ concentration (left axis) and precipitation (right axis) and **(b)** ($PM_{10-2.5}$): $PM_{10}$ at different air quality monitoring sites in Houston. The gray shaded area represents the SDE in Houston.

The PM concentration increased again early on June 26 at the coastal sites, with maximum hourly average $PM_{2.5}$ and $PM_{10}$ concentrations of 115 µg $m^{-3}$ and 301 µg $m^{-3}$, respectively at Oyster Creek and $PM_{2.5}$ concentration of 108 µg $m^{-3}$ at Galveston. The dust plume was then transported inland and was observed at the TCEQ monitoring stations at Deer Park, West Liberty (WL) and Aldine in Houston on June 26. With a transport speed of ~25 km $hr^{-1}$ dust plumes reached these different inland sites at different times of the day depending on

their distance from the coast of Gulf of Mexico. For example, Deer Park, ~53 km from the coast, experienced dust influence at 0300 LST whereas West Liberty and Aldine, both ~86 km from the coast, experienced high PM concentration at 0500 LST. The analysis highlights the coverage of the Saharan dust with inland sites across the Houston metropolitan area. Between June 26 and 27 the coarse fraction ($PM_{10-2.5}$) constituted > 60% of the $PM_{10}$ concentration (Figure 5b) at these sites. It should be noted that the coarse PM constituted the major fraction of $PM_{10}$ (>50%) both at Oyster Creek and Deer Park, even before and after the SDE. This can be attributed to the influence of marine air masses from the Gulf of Mexico which bring in super-micron particles such as sea spray and contributes to coarse fraction of PM at these sites. In addition, a relatively larger variation in the contribution of coarse PM to $PM_{10}$ was observed during the onset and non-event days both at Oyster Creek and Deer Park. This can be linked to the influence of sea spray mixed with fine PM emissions from anthropogenic activities within the city. However, the during the SDE, the transported Saharan dust dominated the anthropogenic PM emissions resulting in more consistent coarse PM to $PM_{10}$ ratio.

To confirm that the increased PM was transported dust and not of local origin, the EF of specific elements in Houston PM was investigated. The EF for the sample collected during the SDE (June 26) was compared with the samples collected prior to the SDE (in the month of May and June prior to the SDE) and post SDE (July). The EF of As, Ba, Co, Zn, Cr, Ni, Sr was significantly enriched (EF >15) in samples collected prior to the SDE, demonstrating the dominance of anthropogenic sources on the elemental composition. At the time of the Saharan dust intrusion, the EF of these elements was reduced by ~90% (Figure S5 – S6). The EF values for Si, Al, Fe were close to unity whereas those for K, Ca, Mg, Mn, Sr were slightly elevated (EF 1-3) (Figure S5). These results are similar to previously reported EFs during Saharan dust events

518 in Houston (Bozlaker et al., 2013), and the Sonoran Desert and the Chihuahuan Desert dust
519 events in the western US (Tong et al., 2012). It should be noted here that due to the limited
520 availability of chemical fingerprints of mineral dust from various source regions, it is still
521 difficult to distinguish the origin of dust based on bulk elemental composition.
522 The $PM_{2.5}$ concentration at all the sites in Houston was significantly higher ($p<0.05$) after June
523 28 compared to that observed prior to the onset of the dust event (Figure S11). The higher
524 concentrations of $PM_{2.5}$ were observed at all the TCEQ monitoring sites till mid-July. This can
525 be attributed to the on-going transport of dust plumes in addition to the recirculation and/or re-
526 suspension of mineral dust in the atmosphere at Houston under dry summer conditions (Ealo et
527 al., 2016). The impact of dust is also affirmed by lower SAE and higher AAE values during this
528 period. In addition, lower EF (As, Ba, Co, Zn, Cr, Ni, Sr) for the $PM_{2.5}$ post SDE also suggests
529 the on-going influence of dust (Figure S6). The evidence that Saharan dust can continue to
530 impact fine particulate matter ($PM_{2.5}$) even beyond the initial SDE is of high relevance for
531 human health and for air quality policy (Jaffe et al., 2023). Resuspended dust in the atmosphere
532 can penetrate deep into the respiratory tracts and can result in long-term chronic health impacts
533 (Xing et al., 2016). This further indicates potential implications of these dust episodes on human
534 health and importance of characterizing long term dust influence in urban areas.

535 **3.4. Aerosol radiative forcing during the 2020 Saharan dust event**

536 Characterization of the impacts of SDE in the US necessitates both an assessment of the
537 surface loading and related human exposure as well as the climate impacts associated with
538 perturbances in regional radiative forcing. The total downwelling and upwelling solar irradiances
539 (direct and diffuse) at the TOA and surface were simulated using SBDART at WL, APP and
540 BND. The results showed that at the TOA the mean total upwelling irradiance increased by 6%,

10% and 4% for WL, APP and BND, respectively during the SDE compared to the non-event days suggesting enhanced scattering due to Saharan dust. Further, net downwelling irradiance at the surface was calculated for each site. For the non-event days, the calculated mean net downwelling irradiance at the surface was 471 $Wm^{-2}$, 476 $Wm^{-2}$ and 446 $Wm^{-2}$ at WL, APP and BND, respectively. The mean net downwelling irradiance at the surface decreased by ~4%, ~4% and ~2% at WL, APP and BND, respectively during the 2020 SDE. This decrease in net downwelling irradiance at the surface was due to the increase in diffuse irradiance (by ~29% at WL, ~52% at APP and ~17% at BND) due to the presence of dust aerosols. The overall uncertainty in the estimated downwelling and upwelling solar irradiances at TOA and surface using the given SBDART configuration (discussed in supplementary section 5.2) is found to be in the range of 10-15% (Alam et al., 2011; Kalluri et al., 2020; Prasad et al., 2007; Valenzuela et al., 2012). This uncertainty in model simulations is associated with the uncertainties in the derivation of AOPs (AOD, SSA and g) from OPAC and the retrieved surface albedo values (Alam et al., 2011; Kalluri et al., 2020; Prasad et al., 2007; Valenzuela et al., 2012). In addition, there were clouds over the study sites during the SDE, which can add some more uncertainty in estimating total downwelling and upwelling irradiances. However, due to the lack of measurements that could be used to constrain the impact of clouds on the derived AOPs, in the OPAC model, we could not estimate the additional uncertainty during cloudy days.

The mean daily ARF at the TOA during the SDE (non-event days) was -9.75 $Wm^{-2}$ (-5.91 $Wm^{-2}$), -17.8 $Wm^{-2}$ (-7.58 $Wm^{-2}$) and -6.65 $Wm^{-2}$ (-3.12 $Wm^{-2}$) at WL, APP and BND, respectively (Figure 6). The corresponding surface ARF values during the SDE (non-event days) were -21.5 $Wm^{-2}$ (-6.96 $Wm^{-2}$), -27.3 $Wm^{-2}$ (-8.42 $Wm^{-2}$), -12.0 $Wm^{-2}$ (-4.14 $Wm^{-2}$) at WL, APP and BND, respectively. The above estimates indicate two-to-three-fold increases in the negative

ARF at TOA and surface from non-event days to SDE (Figure 6). The magnitude of the impact of dust on ARF was lowest at BND. This is related to the difference in plume density and the distance from the dust source at BND relative to the other sites (discussed in detail in section 3.1.1). The difference between the ARF at the TOA and surface is defined as the atmospheric ARF and represents the amount of energy trapped in the atmosphere. The atmospheric ARF during the SDE was estimated to be 11.8 $Wm^{-2}$, 9.47 $Wm^{-2}$, and 5.37 $Wm^{-2}$ at WL, APP and BND, respectively (Figure 6). The estimates showed that the Saharan dust intrusion at these sites resulted in an additional positive atmospheric ARF by 10.7 $Wm^{-2}$, 8.63 $Wm^{-2}$, 4.35 $Wm^{-2}$ at WL, APP and BND, respectively compared to that estimated for non-event days. This change in the atmospheric ARF can affect the thermal structure of the atmosphere and change its thermodynamic state (Asutosh et al., 2022; Yang et al., 2017). The Saharan dust event in 2020 resulted in a ~16% increase in atmospheric temperature and a ~ 2% decrease in the relative humidity over the Atlantic Ocean (Asutosh et al., 2022).

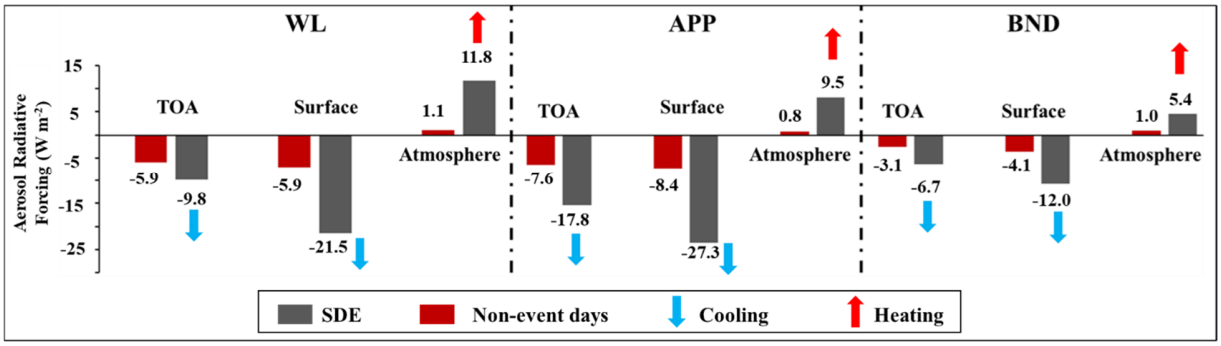


**Figure 6.** Average aerosol radiative forcing at the top of atmosphere (TOA), surface and in the atmosphere during the non-event days and the SDE at WL, APP and BND, respectively.

Previous studies using different modelling approaches for ARF estimation have also reported large negative ARF at TOA, surface and positive atmospheric ARF during SDEs

582 (Córdoba-Jabonero et al., 2021; Gkikas et al., 2018; Kaskaoutis et al., 2019; Mamun et al., 2021;
583 Oduber et al., 2019; Papadimas et al., 2012; Valenzuela et al., 2012). For instance, Kaskaoutis et
584 al. (2019) reported a significant impact of Saharan dust on the radiation budget for cities in
585 Greece, with a large decrease in net downwelling irradiance at the surface (~ -40W $m^{-2}$ to -50
586 $Wm^{-2}$) and at the TOA (~-5 $Wm^{-2}$ to -30 $Wm^{-2}$). This translated to an increase in positive
587 atmospheric ARF by ~ +2 $Wm^{-2}$ to +17 $Wm^{-2}$. Mean ARF values at TOA, surface, and
588 atmosphere of $-12 \pm 11$ $Wm^{-2}$, $-40 \pm 23$ $Wm^{-2}$ and $+29 \pm 25$ $Wm^{-2}$, respectively, were estimated
589 during SDEs in Granada, Spain (Valenzuela et al., 2012). Mishra et al. (2014) reported an
590 atmospheric ARF of +9.4 $Wm^{-2}$ for pure dust aerosol and a maximum of +16.7 $Wm^{-2}$ for
591 polluted dust aerosols over the eastern Mediterranean Basin. The magnitude of the impact of dust
592 on the radiation budget reported in these studies is higher than that observed in the present study
593 (Table 3). This may be attributed to longer transport from the source to the receptor region
594 and/or differences in the ARF modelling approach (Valenzuela et al., 2012).
595 The lower atmospheric heating rate during the 2020 SDE was 0.23 K $day^{-1}$, 0.24 K $day^{-1}$,
596 0.11 K $day^{-1}$ at WL, APP and BND, respectively. This increase in the heating rate due to the
597 presence of Saharan dust aerosols can result in trapping of pollutants in the lower atmosphere by
598 changing regional circulation patterns and strengthening temperature inversions (Yang et al.,
599 2017). Additionally, this heating of the atmosphere can have implications for the hydrological
600 cycle and the development of mesoscale weather phenomena such as convection and sea-breeze
601 patterns whose circulations are driven by horizontal heterogeneities in local-scale thermal
602 contrast (Alamirew et al., 2018; Ge et al., 2014; Sun and Zhao, 2020).

603 **Table 3.** Daily aerosol radiative forcing ($Wm^{-2}$) at the Top of Atmosphere (TOA), Surface, and
604 in the atmosphere and associated heating rates observed over different locations during Saharan
605 dust events.

| ARF ($Wm^{-2}$) | | | Heating rate ($K\ day^{-1}$) | Location | Reference |
|---|---|---|---|---|---|
| TOA | Surface | Atmosphere | | | |
| -9.8 | -21.5 | 11.8 | 0.23 | West Liberty, Texas, US | Present study |
| -17.8 | -27.3 | 9.5 | 0.24 | Appalachian State University, North Carolina, US | Present study |
| -6.7 | -12.0 | 5.4 | 0.11 | Bondville, Illinois, US | Present study |
| -80 | -150 | 70 | - | Atlantic Ocean | (Asutosh et al., 2022) |
| -11.3 | -13.7 | 2.4 | 0.2 | Tropical East Atlantic Ocean | (Mamun et al., 2021) |
| -6.0 | -9.1 | 3.1 | - | Barcelona, Spain | (Córdoba-Jabonero et al., 2021) |
| -84.1 | -164.9 | 80.8 | - | Iberian Peninsula | (Oduber et al., 2019) |
| -13.9 | -43.6 | 28.0 | 0.9 | Mediterranean Basin | (Gkikas et al., 2018) |
| -30.0 | -50.0 | ~20 | 0.5 | Athens, Greece | (Kaskaoutis et al., 2019) |
| -5 | -20 | 15 | 0.14 | Granada, Spain | (Valenzuela et al., 2012) |
| -7 | -21 | 14 | 0.13 | Granada, Spain | (Valenzuela et al., 2012) |
| -6 | -18 | 12 | 0.11 | Granada, Spain | (Valenzuela et al., 2012) |
| -8.1 | -29.1 | 21 | - | Senegal | (Derimian et al., 2008) |

606

607 ## 4. Conclusions

608 The present study shows the impact of the June 2020 Saharan dust event on AOPs measured at
609 three different monitoring stations: WL (southern US), APP (eastern US) and BND (midwestern
610 US). As the Saharan dust was transported across each site, the aerosol concentration increased
611 significantly with a marked increase in scattering (except at BND) and absorption coefficients.
612 The SAE dropped below 0.5 at WL, and APP and below 0.9 at BND. The AAE peaked above 1.4

during the SDE at all the sites. SSAAE values less than 0 indicated the dominance of coarser particles at each site. These results indicate that radiative and air quality SDE impacts can be evaluated using measurements and calculated parameters ($\sigma_{scat}$, SAE, AAE, SSAAE, and PM) from surface aerosol monitoring networks like BC2 and NFAN combined with satellite observations (AOD). The results also show evidence of recirculation and/or re-suspension of dust particles in $PM_{2.5}$ even after the passage of the primary SDE which is of high relevance for public health.

An investigation into the larger climatic impacts of Saharan dust revealed a two-to-three-fold reduction in the ARF at TOA and SURF due to enhanced attenuation of incoming solar radiation by dust aerosols. The Saharan dust intrusion resulted in an additional warming of the atmosphere by 10.7 $Wm^{-2}$, 8.63 $Wm^{-2}$ and 4.35 $Wm^{-2}$ at WL, APP and BND, respectively. In this study, the ARF estimations were performed for clear-sky conditions. It is important to acknowledge that the ARF estimates may be biased due to a lack of consideration of the impact of clouds on certain days. The atmospheric warming during the SDE translated into heating of lower atmosphere at the rate of 0.33 K $day^{-1}$, 0.35 K $day^{-1}$, 0.15 K $day^{-1}$ at WL, APP and BND, respectively. The study demonstrates that the Saharan dust events can have a significant impact on the radiation budget of southern, eastern and midwestern US states. Future climate studies should consider both surface and radiative effects of dust in order to improve the accuracy to predict weather and climate change in the US.

**Data availability**

The BC2 aerosol optical data are available upon request. NFAN aerosol data are available at the World Data Centre for Aerosols archive hosted at NILU: https://ebas.nilu.no. The PM data for the TCEQ sites in Houston-Galveston region is available at the Geographical Texas Air Quality Monitoring viewer (https://www.tceq.texas.gov/gis/geotam-viewer). PM speciation data from the NCAR Regional Air Quality Forecasting System is available upon request. MODIS Level 3 dataset is hosted at Level-1 and Atmosphere Archive & Distribution System (LAADS) Distributed Active Archive Center (DAAC) (https://ladsweb.modaps.eosdis.nasa.gov).

## Author Contributions

M.M., S.S., M.C.G., C.E.M., S.G.V., J.H.F., E.A., J.P.S., S.U. and R.J.S. participated in the field campaign and long-term observations, including measurements and data quality assurance. M.M. performed data analysis. M.M., R.K., K.A.P., M.R. participated in the radiative forcing model runs and interpretations. R.J.S. and S.U. supervised the project and data analysis. M.M. prepared a draft of the manuscript. M.M., S.U., and R.J.S. edited the final version of the manuscript. All authors reviewed the manuscript and provided inputs for data analysis.

## Competing Interest

The authors declare that they have no conflict of interest.

## Acknowledgements

The black and brown carbon (BC2) monitoring in Houston and El Paso in 2020 was financed through the TCEQ (Grant number: 582-20-12102-011). The content, findings, opinions, and conclusions are the work of the authors and do not necessarily represent findings, opinions, or

conclusions of the TCEQ. We appreciate the care and effort Patrick Sheridan (now retired) put into maintaining observations and doing data QA/QC at BND throughout his career. We also acknowledge Patrick Sheridan and Olga Mayol-Bracero for the initial discussions of this Saharan dust event. EA was supported in part by NOAA cooperative agreement NA22OAR4320151. RK works at the National Center for Atmospheric Research, which is sponsored by the National Science Foundation

## 5. References

Alam, K., Trautmann, T., Blaschke, T., 2011. Aerosol optical properties and radiative forcing over mega-city Karachi. Atmos Res 101, 773–782. https://doi.org/10.1016/j.atmosres.2011.05.007

Alamirew, N.K., Todd, M.C., Ryder, C.L., Marsham, J.H., Wang, Y., 2018. The early summertime Saharan heat low: sensitivity of the radiation budget and atmospheric heating to water vapour and dust aerosol. Atmos. Chem. Phys. 18, 1241–1262. https://doi.org/10.5194/acp-18-1241-2018

Anderson, T.L., Ogren, J.A., 1998. Determining aerosol radiative properties using the TSI 3563 Integrating Nephelometer. Aerosol Sci. Technol. 29(1):57–69. https://doi.org/10.1080/02786829808965551

Andrews, E., Sheridan, P.J., Fiebig, M., McComiskey, A., Ogren, J.A., Arnott, P., Covert, D., Elleman, R., Gasparini, R., Collins, D., Jonsson, H., Schmid, B., Wang, J., 2006. Comparison of methods for deriving aerosol asymmetry parameter. J. Geophys. Res. Atmos. 111. https://doi.org/10.1029/2004JD005734

676 Andrews, E., Sheridan, P.J., Ogren, J.A., Hageman, D., Jefferson, A., Wendell, J., Alástuey, A.,
677 Alados-Arboledas, L., Bergin, M., Ealo, M., Hallar, A.G., Hoffer, A., Kalapov, I., Keywood, M.,
678 Kim, J., Kim, S.-W., Kolonjari, F., Labuschagne, C., Lin, N.-H., Macdonald, A., Mayol-Bracero,
679 O.L., McCubbin, I.B., Pandolfi, M., Reisen, F., Sharma, S., Sherman, J.P., Sorribas, M., Sun, J.,
680 2019. Overview of the NOAA/ESRL Federated Aerosol Network. Bull. Am. Meteorol. Soc. 100,
681 123–135. https://doi.org/10.1175/BAMS-D-17-0175.1

682 Asutosh, A., Vinoj, V., Murukesh, N., Ramisetty, R., Mittal, N., 2022. Investigation of June
683 2020 giant Saharan dust storm using remote sensing observations and model reanalysis. Sci. Rep
684 .12, 6114. https://doi.org/10.1038/s41598-022-10017-1

685 Bergstrom, R.W., Pilewskie, P., Russell, P.B., Redemann, J., Bond, T.C., Quinn, P.K., Sierau,
686 B., Physics, S., Sciences, O., Marine, P., Oceanic, N., Science, C., 2007. Spectral absorption
687 properties of atmospheric aerosols. Atmos. Chem. Phys. 5937–5943. https://doi.org/10.5194/acp-
688 7-5937-2007, 2007

689 Bond, T.C., Anderson, T.L., Campbell, D., 1999. Calibration and Intercomparison of Filter-
690 Based Measurements of Visible Light Absorption by Aerosols. Aeros. Sci. Tech. 30, 582–600.
691 https://doi.org/10.1080/027868299304435

692 Bozlaker, A., Prospero, J.M., Fraser, M.P., Chellam, S., 2013. Quantifying the Contribution of
693 Long-Range Saharan Dust Transport on Particulate Matter Concentrations in Houston, Texas,
694 Using Detailed Elemental Analysis. Environ. Sci. Tech. 47, 10179–10187.
695 https://doi.org/10.1021/es4015663

696 Choobari, O.A., Zawar-Reza, P., Sturman, A., 2014. The global distribution of mineral dust and
697 its impacts on the climate system: A review. Atmos. Res. 138, 152–165.
698 https://doi.org/10.1016/j.atmosres.2013.11.007

699 Collaud Coen, M., Weingartner, E., Schaub, D., Hueglin, C., Corrigan, C., Henning, S.,
700 Schwikowski, M., Baltensperger, U., 2004. Saharan dust events at the Jungfraujoch: detection by
701 wavelength dependence of the single scattering albedo and first climatology analysis. Atmos.
702 Chem. Phys. 4, 2465–2480. https://doi.org/10.5194/acp-4-2465-2004

703 Collaud Coen, M., Andrews, E., Alastuey, A., Arsov, T.P., Backman, J., Brem, B.T.,
704 Bukowiecki, N., Couret, C., Eleftheriadis, K., Flentje, H., Fiebig, M., Gysel-Beer, M., Hand,
705 J.L., Hoffer, A., Hooda, R., Hueglin, C., Joubert, W., Keywood, M., Kim, J.E., Kim, S.-W.,
706 Labuschagne, C., Lin, N.-H., Lin, Y., Lund Myhre, C., Luoma, K., Lyamani, H., Marinoni, A.,
707 Mayol-Bracero, O.L., Mihalopoulos, N., Pandolfi, M., Prats, N., Prenni, A.J., Putaud, J.-P., Ries,
708 L., Reisen, F., Sellegri, K., Sharma, S., Sheridan, P., Sherman, J.P., Sun, J., Titos, G., Torres, E.,
709 Tuch, T., Weller, R., Wiedensohler, A., Zieger, P., Laj, P., 2020. Multidecadal trend analysis of
710 in situ aerosol radiative properties around the world. Atmos Chem Phys 20, 8867–8908.
711 https://doi.org/10.5194/acp-20-8867-2020

712 Córdoba-Jabonero, C., Sicard, M., López-Cayuela, M.-Á., Ansmann, A., Comerón, A., Zorzano,
713 M.-P., Rodriguez-Gómez, A., Muñoz-Porcar, C., 2021. Aerosol radiative impact during the
714 summer 2019 heatwave produced partly by an inter-continental Saharan dust outbreak – Part 1:
715 Short-wave dust direct radiative effect. Atmos. Chem. Phys. 21, 6455–6479.
716 https://doi.org/10.5194/acp-21-6455-2021

717 Costabile, F., Barnaba, F., Angelini, F., Gobbi, G.P., 2013. Identification of key aerosol
718 populations through their size and composition resolved spectral scattering and absorption.
719 Atmos. Chem. Phys. 13, 2455–2470. https://doi.org/10.5194/acp-13-2455-2013

720 Davies, N.W., Fox, C., Szpek, K., Cotterell, M.I., Taylor, J.W., Allan, J.D., Williams, P.I.,
721 Trembath, J., Haywood, J.M., Langridge, J.M., 2019. Evaluating biases in filter-based aerosol
722 absorption measurements using photoacoustic spectroscopy. Atmos. Meas. Tech. 12, 3417–3434.
723 https://doi.org/10.5194/amt-12-3417-2019

724 Delene, D.J., Ogren, J.A., 2002. Variability of Aerosol Optical Properties at Four North
725 American Surface Monitoring Sites. J. Atmos. Sci. 59, 1135–1150. https://doi.org/10.1175/1520-
726 0469(2002)059<1135: VOAOPA>2.0.CO;2

727 Denjean, C., Formenti, P., Desboeufs, K., Chevaillier, S., Triquet, S., Maillé, M., Cazaunau, M.,
728 Laurent, B., Mayol-Bracero, O.L., Vallejo, P., Quiñones, M., Gutierrez-Molina, I.E., Cassola, F.,
729 Prati, P., Andrews, E., Ogren, J., 2016. Size distribution and optical properties of African mineral
730 dust after intercontinental transport. J. Geophys. Res. Atmos. 121, 7117–7138.
731 https://doi.org/10.1002/2016JD024783

732 DeMott, P.J., Sassen, K., Poellot, M.R., Baumgardner, D., Rogers, D.C., Brooks, S.D., Prenni,
733 A.J., Kreidenweis, S.M., 2003. African dust aerosols as atmospheric ice nuclei. Geophys. Res.
734 Lett. 30. https://doi.org/10.1029/2003GL017410

735 Derimian, Y., Léon, J.-F., Dubovik, O., Chiapello, I., Tanré, D., Sinyuk, A., Auriol, F., Podvin,
736 T., Brogniez, G., Holben, B.N., 2008. Radiative properties of aerosol mixture observed during
737 the dry season 2006 over M'Bour, Senegal (African Monsoon Multidisciplinary Analysis
738 campaign). J. Geophys. Res. Atmos. 113. https://doi.org/10.1029/2008JD009904

739 Donateo, A., lo Feudo, T., Marinoni, A., Dinoi, A., Avolio, E., Merico, E., Calidonna, C.R.,
740 Contini, D., Bonasoni, P., 2018. Characterization of In Situ Aerosol Optical Properties at Three
741 Observatories in the Central Mediterranean. Atmosphere 9.
742 https://doi.org/10.3390/atmos9100369

743 Dumka, U.C., Saheb, S.D., Kaskaoutis, D.G., Kant, Y., Mitra, D., 2016. Columnar aerosol
744 characteristics and radiative forcing over the Doon Valley in the Shivalik range of northwestern
745 Himalayas. Enviro. Sci. Pollut. Res. 23, 25467–25484. https://doi.org/10.1007/s11356-016-7766-
746 y

747 Ealo, M., Alastuey, A., Ripoll, A., Pérez, N., Minguillón, M.C., Querol, X., Pandolfi, M., 2016.
748 Detection of Saharan dust and biomass burning events using near-real-time intensive aerosol
749 optical properties in the north-western Mediterranean. Atmos. Chem. Phys. 16, 12567–12586.
750 https://doi.org/10.5194/acp-16-12567-2016

751 Evan, A.T., Foltz, G.R., Zhang, D., Vimont, D.J., 2011. Influence of African dust on ocean–
752 atmosphere variability in the tropical Atlantic. Nat. Geosci. 4, 762–765.
753 https://doi.org/10.1038/ngeo1276

754 Farah, A., Villani, P., Rose, C., Conil, S., Langrene, L., Laj, P., Sellegri, K., 2020.
755 Characterization of Aerosol Physical and Optical Properties at the Observatoire Pérenne de
756 l'Environnement (OPE) Site. Atmosphere (Basel) 11. https://doi.org/10.3390/atmos11020172

757 Fernández, A.J., Molero, F., Salvador, P., Revuelta, A., Becerril-Valle, M., Gómez-Moreno, F.J.,
758 Artíñano, B., Pujadas, M., 2017. Aerosol optical, microphysical and radiative forcing properties
759 during variable intensity African dust events in the Iberian Peninsula. Atmos. Res. 196, 129–141.
760 https://doi.org/10.1016/j.atmosres.2017.06.019

761 Francis, D., Chaboureau, J.-P., Nelli, N., Cuesta, J., Alshamsi, N., Temimi, M., Pauluis, O., Xue,
762 L., 2021. Summertime dust storms over the Arabian Peninsula and impacts on radiation,
763 circulation, cloud development and rain. Atmos. Res. 250, 105364.
764 https://doi.org/10.1016/j.atmosres.2020.105364

765 Francis, D., Fonseca, R., Nelli, N., Cuesta, J., Weston, M., Evan, A., Temimi, M., 2020. The
766 Atmospheric Drivers of the Major Saharan Dust Storm in June 2020. Geophys. Res. Lett. 47,
767 e2020GL090102. https://doi.org/10.1029/2020GL090102

768 Ge, C., Wang, J., Reid, J.S., 2014. Mesoscale modeling of smoke transport over the Southeast
769 Asian Maritime Continent: coupling of smoke direct radiative effect below and above the low-
770 level clouds. Atmos. Chem. Phys. 14, 159–174. https://doi.org/10.5194/acp-14-159-2014

771 Gkikas, A., Obiso, V., Pérez Garcia-Pando, C., Jorba, O., Hatzianastassiou, N., Vendrell, L.,
772 Basart, S., Solomos, S., Gassó, S., Baldasano, J.M., 2018. Direct radiative effects during intense
773 Mediterranean desert dust outbreaks. Atmos. Chem. Phys. 18, 8757–8787.
774 https://doi.org/10.5194/acp-18-8757-2018

775 Gómez-Amo, J.L., Pinti, V., di Iorio, T., di Sarra, A., Meloni, D., Becagli, S., Bellantone, V.,
776 Cacciani, M., Fuà, D., Perrone, M.R., 2011. The June 2007 Saharan dust event in the central
777 Mediterranean: Observations and radiative effects in marine, urban, and sub-urban environments.
778 Atmos. Environ. 45, 5385–5393. https://doi.org/10.1016/j.atmosenv.2011.06.045

779 Haywood, J.M., Allan, R.P., Culverwell, I., Slingo, T., Milton, S., Edwards, J., Clerbaux, N.,
780 2005. Can desert dust explain the outgoing longwave radiation anomaly over the Sahara during
781 July 2003? J. Geophys. Res. Atmos. 110. https://doi.org/10.1029/2004JD005232

Hess, M., Koepke, P., Schult, I., 1998. Optical Properties of Aerosols and Clouds: The Software Package OPAC. Bull. Am. Meteorol. Soc. 79, 831–844. https://doi.org/10.1175/1520-0477(1998)079<0831: OPOAAC>2.0.CO;2

Horvath, H., Alados Arboledas, L., Olmo Reyes, F.J., 2018. Angular scattering of the Sahara dust aerosol. Atmos. Chem. Phys. 18, 17735–17744. https://doi.org/10.5194/acp-18-17735-2018

Horvath, H., Kasahara, M., Tohno, S., Olmo, F.J., Lyamani, H., Alados-Arboledas, L., Quirantes, A., Cachorro, V., 2016. Relationship between fraction of backscattered light and asymmetry parameter. J. Aerosol. Sci.91, 43–53. https://doi.org/10.1016/j.jaerosci.2015.09.003

Jaffe, D. A., Miller, C., Thompson, K., Finley, B., Nelson, M., Ouimette, J., Andrews, E., 2023. An evaluation of the U.S. EPA's correction equation for PurpleAir sensor data in smoke, dust, and wintertime urban pollution events. Atmos. Meas. Tech. 16, 1311–1322. https://doi.org/10.5194/amt-16-1311-2023

Jickells, T.D., An, Z.S., Andersen, K.K., Baker, A.R., Bergametti, G., Brooks, N., Cao, J.J., Boyd, P.W., Duce, R.A., Hunter, K.A., Kawahata, H., Kubilay, N., laRoche, J., Liss, P.S., Mahowald, N., Prospero, J.M., Ridgwell, A.J., Tegen, I., Torres, R., 2005. Global Iron Connections Between Desert Dust, Ocean Biogeochemistry, and Climate. Science (1979) 308, 67–71. https://doi.org/10.1126/science.1105959

Jish Prakash, P., Stenchikov, G., Kalenderski, S., Osipov, S., Bangalath, H., 2015. The impact of dust storms on the Arabian Peninsula and the Red Sea. Atmos. Chem. Phys. 15, 199–222. https://doi.org/10.5194/acp-15-199-2015

Kalluri, R.O.R., Gugamsetty, B., Kotalo, R.G., Thotli, L.R., Tandule, C.R., Akkiraju, B., 2020. Long-term (2008–2017) analysis of atmospheric composite aerosol and black carbon radiative

804 forcing over a semi-arid region in southern India: Model results and ground measurement.
805 Atmos. Environ. 240, 117840. https://doi.org/10.1016/j.atmosenv.2020.117840

806 Kaskaoutis, D.G., Sinha, P.R., Vinoj, V., Kosmopoulos, P.G., Tripathi, S.N., Misra, A.,
807 Sharma, M., Singh, R.P., 2013. Aerosol properties and radiative forcing over Kanpur
808 during severe aerosol loading conditions. Atmos. Environ. 79, 7–19.
809 https://doi.org/10.1016/j.atmosenv.2013.06.020

810 Kaskaoutis, D.G., Dumka, U.C., Rashki, A., Psiloglou, B.E., Gavriil, A., Mofidi, A., Petrinoli,
811 K., Karagiannis, D., Kambezidis, H.D., 2019. Analysis of intense dust storms over the eastern
812 Mediterranean in March 2018: Impact on radiative forcing and Athens air quality. Atmos.
813 Environ. 209, 23–39. https://doi.org/10.1016/j.atmosenv.2019.04.025

814 Kirchstetter, T.W., Novakov, T., Hobbs, P. v, 2004. Evidence that the spectral dependence of
815 light absorption by aerosols is affected by organic carbon. J. Geophys. Res. Atmos. 109.
816 https://doi.org/10.1029/2004JD004999

817 Kumar, S., Kaskaoutis, D.G., Singh, R.P., Singh, R.K., Mishra, A.K., Srivastava,
818 M.K., Singh, A.K., 2015. Meteorological, atmospheric and climatic perturbations
819 during major dust storms over Indo-Gangetic basin. Aeol. Res. 17, 15–31.
820 https://doi.org/10.1016/j.aeolia.2015.01.006

821 Li, L., Li, Z., Chang, W., Ou, Y., Goloub, P., Li, C., Li, K., Hu, Q., Wang, J., Wendisch, M.,
822 2020. Aerosol solar radiative forcing near the Taklimakan Desert based on radiative transfer and
823 regional meteorological simulations during the Dust Aerosol Observation-Kashi campaign.
824 Atmos. Chem. Phys. 20, 10845–10864. https://doi.org/10.5194/acp-20-10845-2020

825 Mamun, A., Chen, Y., Liang, J., 2021. Radiative and cloud microphysical effects of the Saharan
826 dust simulated by the WRF-Chem model. J. Atmos. Sol. Terr. Phys. 219, 105646.
827 https://doi.org/10.1016/j.jastp.2021.105646

828 May, N.W., Bernays, N., Farley, R., Zhang, Q., Jaffe, D.A., 2023. Intensive aerosol properties of
829 boreal and regional biomass burning aerosol at Mt. Bachelor Observatory: larger and black
830 carbon (BC)-dominant particles transported from Siberian wildfires. Atmos. Chem. Phys. 23,
831 2747–2764. https://doi.org/10.5194/acp-23-2747-2023

832 McFarlane, S.A., Kassianov, E.I., Barnard, J., Flynn, C., Ackerman, T.P., 2009. Surface
833 shortwave aerosol radiative forcing during the Atmospheric Radiation Measurement Mobile
834 Facility deployment in Niamey, Niger. J. Geophys. Res. Atmos. 114.
835 https://doi.org/10.1029/2008JD010491

836 Miller, R.L., Tegen, I., Perlwitz, J., 2004. Surface radiative forcing by soil dust aerosols and the
837 hydrologic cycle. J. Geophys. Res. Atmos. 109. https://doi.org/10.1029/2003JD004085

838 Mishra, A.K., Klingmueller, K., Fredj, E., Lelieveld, J., Rudich, Y., Koren, I., 2014. Radiative
839 signature of absorbing aerosol over the eastern Mediterranean Basin. Atmos. Chem. Phys. 14,
840 7213–7231. https://doi.org/10.5194/acp-14-7213-2014

841 Moosmüller, H., Chakrabarty, R.K., 2011. Technical Note: Simple analytical relationships
842 between Ångström coefficients of aerosol extinction, scattering, absorption, and single scattering
843 albedo. Atmos. Chem. Phys. 11, 10677–10680. https://doi.org/10.5194/acp-11-10677-2011

844 Müller, T., Laborde, M., Kassell, G., Wiedensohler, A., 2011. Design and performance of a
845 three-wavelength LED-based total scatter and backscatter integrating nephelometer. Atmos.
846 Meas. Tech. 4, 1291–1303. https://doi.org/10.5194/amt-4-1291-2011

847 Nicolás, J.F., Castañer, R., Galindo, N., Yubero, E., Crespo, J., Clemente, A., 2019. Analysis of
848 aerosol scattering properties and PM10 concentrations at a mountain site influenced by mineral
849 dust transport. Atmos. Environ. 213, 250–257. https://doi.org/10.1016/j.atmosenv.2019.06.017

850 Oduber, F., Calvo, A.I., Blanco-Alegre, C., Castro, A., Nunes, T., Alves, C., Sorribas, M.,
851 Fernández-González, D., Vega-Maray, A.M., Valencia-Barrera, R.M., Lucarelli, F., Nava, S.,
852 Calzolai, G., Alonso-Blanco, E., Fraile, B., Fialho, P., Coz, E., Prevot, A.S.H., Pont, V., Fraile,
853 R., 2019. Unusual winter Saharan dust intrusions at Northwest Spain: Air quality, radiative and
854 health impacts. Sci. Total Environ. 669, 213–228. https://doi.org/10.1016/j.scitotenv.2019.02.305

855 Ogren, J.A., 2010. Comment on "Calibration and Intercomparison of Filter-Based Measurements
856 of Visible Light Absorption by Aerosols." Aeros. Sci. Tech. 44, 589–591.
857 https://doi.org/10.1080/02786826.2010.482111

858 Ogren, J.A., Andrews, E., McComiskey, A., Sheridan, P., Jefferson, A., Fiebig, M., 2006. New
859 insights into aerosol asymmetry parameter, in: Proceedings of the 16th ARM Science Team
860 Meeting, Albuquerque, NM, USA.

861 Ogren, J.A., Wendell, J., Andrews, E., Sheridan, P.J., 2017. Continuous light absorption
862 photometer for long-term studies. Atmos. Meas. Tech. 10, 4805–4818.
863 https://doi.org/10.5194/amt-10-4805-2017

864 Pace, G., di Sarra, A., Meloni, D., Piacentino, S., Chamard, P., 2006. Aerosol optical properties
865 at Lampedusa (Central Mediterranean). 1. Influence of transport and identification of different
866 aerosol types. Atmos. Chem. Phys. 6, 697–713. https://doi.org/10.5194/acp-6-697-2006

867 Papadimas, C.D., Hatzianastassiou, N., Matsoukas, C., Kanakidou, M., Mihalopoulos, N.,
868 Vardavas, I., 2012. The direct effect of aerosols on solar radiation over the broader

869 Mediterranean Basin. Atmos. Chem. Phys. 12, 7165–7185. https://doi.org/10.5194/acp-12-7165-
870 2012

871 Petzold, A., Rasp, K., Weinzierl, B., Esselborn, M., Hamburger, T., DöRNBRACK, A., Kandler,
872 K., SchuüTZ, L., Knippertz, P., Fiebig, M., Virkkula, A., 2009. Saharan dust absorption and
873 refractive index from aircraft-based observations during SAMUM 2006. Tellus B 61, 118–130.
874 https://doi.org/10.1111/j.1600-0889.2008.00383.x

875 Prasad, A.K., Singh, S., Chauhan, S.S., Srivastava, M.K., Singh, R.P., Singh, R., 2007. Aerosol
876 radiative forcing over the Indo-Gangetic plains during major dust storms. Atmos. Environ. 41,
877 6289–6301. https://doi.org/10.1016/j.atmosenv.2007.03.060

878 Prospero, J.M., Collard, F.-X., Molinié, J., Jeannot, A., 2014. Characterizing the annual cycle of
879 African dust transport to the Caribbean Basin and South America and its impact on the
880 environment and air quality. Global Biogeochem. Cycles 28, 757–773.
881 https://doi.org/10.1002/2013GB004802

882 Pu, B., Jin, Q., 2021. A Record-Breaking Trans-Atlantic African Dust Plume Associated with
883 Atmospheric Circulation Extremes in June 2020. Bull. Am. Meteorol. Soc. 102, E1340–E1356.
884 https://doi.org/10.1175/BAMS-D-21-0014.1

885 Raj, J., Bangalath, H.K., Stenchikov, G., 2019. West African Monsoon: current state and future
886 projections in a high-resolution AGCM. Clim. Dyn. 52, 6441–6461.
887 https://doi.org/10.1007/s00382-018-4522-7

888 Ramanathan, V., Crutzen, P.J., Kiehl, J.T., Rosenfeld, D., 2001. Aerosols, Climate, and the
889 Hydrological Cycle. Science (1979) 294, 2119–2124. https://doi.org/10.1126/science.1064034

Ricchiazzi, P., Yang, S., Gautier, C., Sowle, D., 1998. SBDART: A Research and Teaching Software Tool for Plane-Parallel Radiative Transfer in the Earth's Atmosphere. Bull. Am. Meteorol. Soc. 79, 2101–2114. https://doi.org/10.1175/1520-0477(1998)079<2101: SARATS>2.0.CO;2

Ryder, C.L., Highwood, E.J., Rosenberg, P.D., Trembath, J., Brooke, J.K., Bart, M., Dean, A., Crosier, J., Dorsey, J., Brindley, H., Banks, J., Marsham, J.H., McQuaid, J.B., Sodemann, H., Washington, R., 2013. Optical properties of Saharan dust aerosol and contribution from the coarse mode as measured during the Fennec 2011 aircraft campaign. Atmos. Chem. Phys. 13, 303–325. https://doi.org/10.5194/acp-13-303-2013

Sannino, A., Amoruso, S., Damiano, R., Scollo, S., Sellitto, P., Boselli, A., 2022. Optical and microphysical characterization of atmospheric aerosol in the Central Mediterranean during simultaneous volcanic ash and desert dust transport events. Atmos. Res. 271, 106099. https://doi.org/10.1016/j.atmosres.2022.106099

Schuster, G.L., Dubovik, O., Holben, B.N., 2006. Angstrom exponent and bimodal aerosol size distributions. J. Geophys. Res. Atmos. 111. https://doi.org/10.1029/2005JD006328

Sherman, J.P., Sheridan, P.J., Ogren, J.A., Andrews, E., Hageman, D., Schmeisser, L., Jefferson, A., Sharma, S., 2015. A multi-year study of lower tropospheric aerosol variability and systematic relationships from four North American regions. Atmos. Chem. Phys. 15, 12487–12517. https://doi.org/10.5194/acp-15-12487-2015

Shrestha, S., Zhou, S., Mehra, M., Guagenti, M.C., Yoon, S., Alvarez, S.L., Guo, F., Chao, C.-Y., Flynn III, J.H., Wang, Y., Griffin, R.J., Usenko, S., Sheesley, R.J., 2023. Evaluation of aerosol- and gas-phase tracers for identification of transported biomass burning emissions in an

912 industrially influenced location in Texas, USA. EGUsphere [preprint] 2023, 1–33.
913 https://doi.org/10.5194/egusphere-2023-367

914 Song, Q., Zhang, Z., Yu, H., Kato, S., Yang, P., Colarco, P., Remer, L.A., Ryder, C.L., 2018. Net
915 radiative effects of dust in the tropical North Atlantic based on integrated satellite observations
916 and in situ measurements. Atmos. Chem. Phys. 18, 11303–11322. https://doi.org/10.5194/acp-
917 18-11303-2018

918 Sorribas, M., Adame, J.A., Andrews, E., Yela, M., 2017. An anomalous African dust event and
919 its impact on aerosol radiative forcing on the Southwest Atlantic coast of Europe in February
920 2016. Sci. Total Environ. 583, 269–279. https://doi.org/10.1016/j.scitotenv.2017.01.064

921 Sorribas, M., Andrews, E., Ogren, J.A., del Águila, A., Fraile, R., Sheridan, P., Yela, M., 2019.
922 Climatological study for understanding the aerosol radiative effects at southwest Atlantic coast
923 of Europe. Atmos. Environ. 205, 52–66. https://doi.org/10.1016/j.atmosenv.2019.02.017

924 Soupiona, O., Papayannis, A., Kokkalis, P., Foskinis, R., Sánchez Hernández, G., Ortiz-
925 Amezcua, P., Mylonaki, M., Papanikolaou, C.-A., Papagiannopoulos, N., Samaras, S., Groß, S.,
926 Mamouri, R.-E., Alados-Arboledas, L., Amodeo, A., Psiloglou, B., 2020. EARLINET
927 observations of Saharan dust intrusions over the northern Mediterranean region (2014–2017):
928 properties and impact on radiative forcing. Atmos. Chem. Phys. 20, 15147–15166.
929 https://doi.org/10.5194/acp-20-15147-2020

930 Sun, Y., Zhao, C., 2020. Influence of Saharan Dust on the Large-Scale Meteorological
931 Environment for Development of Tropical Cyclone Over North Atlantic Ocean Basin. J.
932 Geophys. Res. Atmos. 125, e2020JD033454. https://doi.org/10.1029/2020JD033454

933 Taylor, M.A., Whyte, F.S., Stephenson, T.S., Campbell, J.D., 2013. Why dry? Investigating the
934 future evolution of the Caribbean Low-Level Jet to explain projected Caribbean drying.
935 International J. of Climatology 33, 784–792. https://doi.org/10.1002/joc.3461

936 Titos, G., Ealo, M., Pandolfi, M., Pérez, N., Sola, Y., Sicard, M., Comerón, A., Querol, X.,
937 Alastuey, A., 2017. Spatiotemporal evolution of a severe winter dust event in the western
938 Mediterranean: Aerosol optical and physical properties. J. Geophys. Res. Atmos. 122, 4052–
939 4069. https://doi.org/10.1002/2016JD026252

940 Tong, D.Q., Dan, M., Wang, T., Lee, P., 2012. Long-term dust climatology in the western United
941 States reconstructed from routine aerosol ground monitoring. Atmos. Chem. Phys. 12, 5189–
942 5205. https://doi.org/10.5194/acp-12-5189-2012

943 Torres-Delgado, E., Baumgardner, D., Mayol-Bracero, O.L., 2021. Measurement report: Impact
944 of African aerosol particles on cloud evolution in a tropical montane cloud forest in the
945 Caribbean. Atmos. Chem. Phys. 21, 18011–18027. https://doi.org/10.5194/acp-21-18011-2021.

946 Valenzuela, A., Olmo, F.J., Lyamani, H., Antón, M., Quirantes, A., Alados-Arboledas, L., 2012.
947 Aerosol radiative forcing during African desert dust events (2005–2010) over Southeastern
948 Spain. Atmos. Chem. Phys. 12, 10331–10351. https://doi.org/10.5194/acp-12-10331-2012

949 Valenzuela, A., Olmo, F.J., Lyamani, H., Antón, M., Titos, G., Cazorla, A., Alados-Arboledas,
950 L., 2015. Aerosol scattering and absorption Angström exponents as indicators of dust and dust-
951 free days over Granada (Spain). Atmos. Res. 154, 1–13.
952 https://doi.org/10.1016/j.atmosres.2014.10.015

WMO, 2011: WMO/GAW standard operating procedures for in-situ measurements of aerosol mass concentration, light scattering, and light absorption. World Meteorological Organization GAW Rep. 200, 130 pp. http://library.wmo.int/pmb_ged/gaw_200.pdf.

Xing, Y.H., Xu, Y.H., Shi, M.H., Lian YX, 2016. The impact of PM2.5 on the human respiratory system. Journal of Thoracic Disease 8, 69–74.

Yang, Y., Russell, L.M., Lou, S., Liao, H., Guo, J., Liu, Y., Singh, B., Ghan, S.J., 2017. Dust-wind interactions can intensify aerosol pollution over eastern China. Nat Commun 8, 15333. https://doi.org/10.1038/ncomms15333

Yu, H., Chin, M., Bian, H., Yuan, T., Prospero, J.M., Omar, A.H., Remer, L.A., Winker, D.M., Yang, Y., Zhang, Y., Zhang, Z., 2015. Quantification of trans-Atlantic dust transport from seven-year (2007–2013) record of CALIPSO lidar measurements. Remote Sens. Environ. 159, 232–249. https://doi.org/10.1016/j.rse.2014.12.010

Yu, H., Tan, Q., Zhou, L., Zhou, Y., Bian, H., Chin, M., Ryder, C.L., Levy, R.C., Pradhan, Y., Shi, Y., Song, Q., Zhang, Z., Colarco, P.R., Kim, D., Remer, L.A., Yuan, T., Mayol-Bracero, O., Holben, B.N., 2021. Observation and modeling of the historic ``Godzilla'' African dust intrusion into the Caribbean Basin and the southern US in June 2020. Atmos. Chem. Phys. 21, 12359–12383. https://doi.org/10.5194/acp-21-12359-2021

Yu, H., Zhang, Z., 2013. New Directions: Emerging satellite observations of above-cloud aerosols and direct radiative forcing. Atmos. Environ. 72, 36–40. https://doi.org/10.1016/j.atmosenv.2013.02.017

973 Yuan, T., Oreopoulos, L., Zelinka, M., Yu, H., Norris, J.R., Chin, M., Platnick, S., Meyer, K.,
974 2016. Positive low cloud and dust feedbacks amplify tropical North Atlantic Multidecadal
975 Oscillation. Geophys. Res. Lett. 43, 1349–1356. https://doi.org/10.1002/2016GL067679